
# Rolling, tilting and spinning spherical wheels: Analytical results using the brush theory

# Rolling, tilting and spinning spherical wheels: analytical results using the brush theory

Luigi Romano*[a], Francesco Timpone[b], Fredrik Bruzelius[a,c], and Bengt Jacobson[a]

[a]Department of Mechanics and Maritime Sciences, Chalmers University of Technology, Hörsalsvägen 7A, 412 96 Gothenburg, Sweden
[b]Department of Industrial Engineering, University of Naples Federico II, Naples, Italy
[c]Driver and Vehicle, VTI Swedish National Road and Transport Research Institute, Box 8072, 402 78 Gothenburg, Sweden

**Abstract**

This paper investigates the rolling dynamics of spherical wheels using the theoretical framework provided by the brush models. The analysis is mainly conducted under the assumption of vanishing sliding inside the contact patch. Different types of kinematics are considered: simply rolling wheels, rolling and tilting, and purely spinning. For the first two cases, a complete solution is derived concerning both the steady-state and transient behaviours. Some qualitative trends for the forces and moments generated inside the contact patch are then provided when accounting for limited friction. For the case of a purely spinning spherical wheel, it is shown that steady-state conditions are never possible owing to the assumption of vanishing sliding. Moreover, it is demonstrated that the shear stresses acting inside the contact patch grow unbounded if the additional contribution relating to the deflection of the bristle is not taken into account when calculating the total sliding velocity. In this case, a stationary solution may be eventually recovered as an asymptotic distribution only by assuming limited friction inside the contact patch.

## Keywords

Rolling contact; transient rolling; brush models; spherical wheels; spherical robots; friction models

## 1 Introduction

The rolling dynamics of omnidirectional spherical robots and wheels have attracted numerous researchers in the last few years [1–4]. In this context, a crucial assumption made in many works is that of *no-slip* conditions for the single contact point between the rolling sphere and its supporting plane [5–7]. In reality, the contact between rolling bodies takes place inside a small, well-defined area, known as the *contact patch*. During the rolling, friction forces induced by the local contact between the surfaces of the bodies arise, producing ultimately the relative motion [8–11].

When the contact patch is relatively small, the sliding friction forces originating from the mutual contact between rolling bodies may still be modelled successfully using the classical one-dimensional Coulomb friction law. However, for many deformable bodies frequently encountered both in the literature and in practical applications, the assumption of a single contact point, or, equivalently, sufficiently small contact patch, does not generally hold. Some emblematic examples of mechanical systems for which this approximation fails include wobblestones, Celtic stones and rattlebacks [12, 13], billiard balls, railway wheels [14–17] and pneumatic tyres [18, 19]. Therefore, during the last few years, a great deal of research has been devoted to the establishment and refinement of appropriate friction models to describe the mutual interaction happening between deformable bodies.

Contensou firstly attempted the development of approximated models to describe the generation mechanism of friction forces [20]. Specifically, he studied mechanical systems subjected to large spins, and derived an integral description of the forces acting at the contact patch under the assumption of full sliding taking place inside a circular area. Later on, Zhuravlev provided exact analytical expressions

*Corresponding author. Email: luigi.romano@chalmers.se.

for the friction forces and moment, along with Padé approximations to be more conveniently used in simulations [21, 22]. This research direction was also explored by Kireenkov, who derived more accurate descriptions in terms of second-order Padé approximants, and took also into account the effect of rolling resistance [23, 24]. Other approximations, based for example on Taylor expansion or polynomial functions, were instead proposed in [25, 26].

In spite of the significant number of papers dealing with rolling contact problems, transient phenomena are however still poorly understood. More specifically, whilst these may be studied in detail using sophisticated models relying on the complete theory of elasticity [27–29], closed-form solutions are rarely available due to the complexity of the formulation. Indeed, even the simplest case of pure longitudinal slip leads to a complicated Hilbert problem that would eventually require a numerical approach, as discovered by Kalker in his pioneering works on the subject [30, 31]. Moreover, Kalker's studies were conducted under the assumption of line contact, which may be a sufficiently good approximation when dealing with railway wheel and tyre dynamics, but would certainly fail for omnidirectional rolling spheres.

On the other hand, the theoretical framework provided by the simpler *brush models* [18, 32–35] is well capable of handling omnidirectional rolling contact for spherical wheels, providing analytical solutions for the shear stresses arising inside the contact patch for a vast combination of cases, even in transient conditions [36]. Indeed, according to the brush theory, a spherical wheel may be modelled as a rigid body equipped with bristles that deform in longitudinal and lateral directions inside the contact patch. Moreover, since the constitutive relationship is assumed to hold only locally, the governing partial differential equations (PDEs) are linear transport equations expressed according to the Eulerian representation.

Hence, this paper aims to investigate the rolling dynamics of spherical wheels and robots according to the brush formulation. Indeed, even though the brush models were originally developed to cope with the steady-state rolling motion of railway wheels and pneumatic tyres under the assumption of small camber angles, their applicability has been successfully extended to other famous problems studied in contact mechanics and machine theory. For example, Romano et al. [37–39] have extensively analysed the transient dynamics of the pneumatic tyre when subjected to large turning speeds and camber angles. In a recent series of papers, Frendo and Bucchi [40–42] have investigated the problem of flat belt transmission from the perspective of the brush models, showing that they also outperform other creep-law-based formulations.

Owing to their versatility, the brush models are hence employed in this paper to analyse the stationary and transient dynamics of rolling spherical wheels. The manuscript is organised as follows: Sect. 2 states the main assumption of the model and introduces the governing equations of a rolling spherical wheel, together with the needed boundary (BCs) and initial conditions (ICs). In Sect. 3, the stationary and transient problems for a rolling sphere with no tilting are solved using the method of characteristics for linear PDEs. Fundamental insights about the existence and uniqueness of the solutions are also provided based on the theory of characteristic equations and other classic results which relate to the famous Cauchy-Kovalevskaya theorem [51–53]. For the steady-state dynamics, explicit solutions for the deflection of the bristles are provided for different possible combinations of rolling speeds. In Sect. 4, the more general situation of a rolling and tilting spherical wheel is explored. With the same approach used in Sect. 3, the steady-state and transient dynamics are analysed separately, owing to the assumption of a sufficiently large tilting radius. Section 5 is then dedicated to the situation of a purely spinning spherical wheel. It is shown that steady-state conditions are never possible under the assumption of vanishing sliding. Moreover, the implications of neglecting second-order terms in the calculation of the sliding velocity are discussed and exemplified. Some examples for the steady-state forces and moment generated during the rolling of the spherical wheel are then provided in Sect. 6. The main conclusions are finally drawn in Sect. 7, along with a discussion on the results advocated in the paper. Appendices A, B and C contain additional results concerning the calculation of the velocity of the contact patch, an application of the energy method to the governing PDEs of the brush models, and analytical representation formulae for their solutions.

## 2 Governing equations of a rolling and sliding spherical wheel

In this paper, it is assumed that the spherical wheel rolls over a contact plane $\mathit{\Pi} = \{\boldsymbol{x} \in \mathbb{R}^3 \mid z = 0\}$. Both the spherical wheel and the contact plane are assumed to be homogeneous and isotropic. The rolling contact takes place inside the contact patch, defined mathematically as a compact set $\mathscr{P}$, with interior and boundary denoted by $\mathring{\mathscr{P}}$ and $\partial\mathscr{P}$, respectively. The contact patch may generally be time-varying, i.e. $\mathscr{P} = \mathscr{P}(t)$, $\partial\mathscr{P} = \partial\mathscr{P}(t)$ and $\mathring{\mathscr{P}} = \mathring{\mathscr{P}}(t)$, even though the explicit dependence upon the time variable $t$

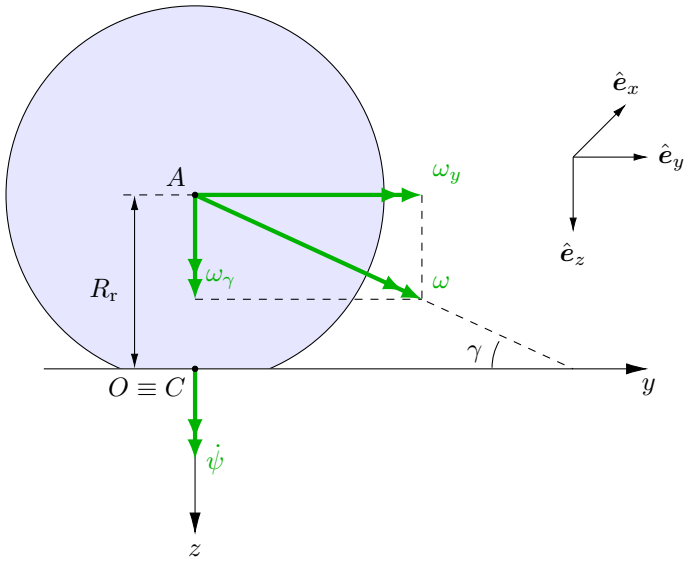


Figure 1: Spherical wheel reference frame with angular velocities.

is often omitted for the sake of readability; for a time-varying contact patch, the initial conditions are denoted as $\mathscr{P}_0 \triangleq \mathscr{P}(0)$, $\partial\mathscr{P}_0 \triangleq \partial\mathscr{P}(0)$ and $\mathring{\mathscr{P}}_0 \triangleq \mathring{\mathscr{P}}(0)$.

A reference frame $(O; x, y, z)$ with unit vectors $(\hat{\boldsymbol{e}}_x, \hat{\boldsymbol{e}}_y, \hat{\boldsymbol{e}}_z)$ is introduced whose origin $O$ is contact-fixed, that is attached to the contact patch $\mathscr{P}$. In this paper, the origin $O$ coincides with the centre of the contact patch $C$. The coordinate system is oriented according to the SAE convention: the $z$ axis is directed downwards, perpendicularly to $\Pi$ and pointing inside the contact plane, the $x$ and $y$ axes are parallel to $\Pi$, and oriented such that the reference frame is right-handed. They do not rotate through rotation of the spherical wheel about axes parallel to $\Pi$, but only through rotation about the $z$ axis due to spinning of the sphere. In the contact patch fixed reference system, the rotational velocity of the spherical wheel is thus given by $\boldsymbol{\omega}(t) = \omega_x(t)\hat{\boldsymbol{e}}_x + \omega_y(t)\hat{\boldsymbol{e}}_y + \omega_\gamma(t)\hat{\boldsymbol{e}}_z$, where $\omega_\gamma(t)$ is calculated as the difference between the rotational speed $\omega_z(t)$ around the $z$-axis and the spin speed $\dot{\psi}(t)$, i.e. $\omega_\gamma(t) = \omega_z(t) - \dot{\psi}(t)$. Hence, the term $\omega_\gamma(t)$ may be generally interpreted as a *tilting* angular speed.

In *pure rolling* conditions, the point $O \equiv C$ moves with absolute rolling velocity $\boldsymbol{V}_O(t) \equiv \boldsymbol{V}_C(t) \equiv \boldsymbol{V}_\mathrm{r}(t) = \begin{bmatrix}-\omega_y(t) & \omega_x(t)\end{bmatrix}^\mathrm{T} R_\mathrm{r}$, where $R_\mathrm{r}$ the *pure rolling radius* [32]. For a rolling spherical wheel, the pure rolling radius may be fairly assumed to be coincident with the deformed radius. The reference frame for the spherical wheel, together with its angular velocities, is shown in Fig. 1 (for simplicity, it has been assumed $\omega_x(t) = 0$).

The part of the spherical wheel contacting the plane $\Pi$ is equipped with bristles which undergo a deformation described by the tangential vector displacement $\boldsymbol{u}_{\boldsymbol{t}}(\boldsymbol{x}, t) = u_x(\boldsymbol{x}, t)\hat{\boldsymbol{e}}_x + u_y(\boldsymbol{x}, t)\hat{\boldsymbol{e}}_y$. The roots of the bristles attached to the rolling sphere travel inside $\mathscr{P}$ with tangential velocity given by the vector field $\mathrm{d}\boldsymbol{x}/\,\mathrm{d}t = \boldsymbol{v}_{\boldsymbol{t}}(\boldsymbol{x}, t) = v_x(\boldsymbol{x}, t)\hat{\boldsymbol{e}}_x + v_y(\boldsymbol{x}, t)\hat{\boldsymbol{e}}_y$ and are subjected to tangential forces per unit of area $\boldsymbol{q}_{\boldsymbol{t}}(\boldsymbol{x}, t) = q_x(\boldsymbol{x}, t)\hat{\boldsymbol{e}}_x + q_y(\boldsymbol{x}, t)\hat{\boldsymbol{e}}_y$. In this paper, the tangential shear stress is assumed to be related to the displacement of the bristle through $\boldsymbol{q}_{\boldsymbol{t}}(\boldsymbol{x}, t) = k\boldsymbol{u}_{\boldsymbol{t}}(\boldsymbol{x}, t)$, where $k$ represents a constant stiffness per unit of volume.

Owing to this premises, the relative *micro-sliding velocity* between the tip of the bristles and the contact plane, denoted by $\boldsymbol{v}_\mathrm{s}(\boldsymbol{x}, t) = v_{\mathrm{s}x}(\boldsymbol{x}, t)\hat{\boldsymbol{e}}_x + v_{\mathrm{s}y}(\boldsymbol{x}, t)\hat{\boldsymbol{e}}_y$, reads

$$\boldsymbol{v}_\mathrm{s}(\boldsymbol{x}, t) = \boldsymbol{V}_\mathrm{s}(t) + \mathbf{A}_{\omega_z}(t)\big(\boldsymbol{x} + \chi_\psi(t)\boldsymbol{u}_{\boldsymbol{t}}(\boldsymbol{x}, t)\big) + \frac{\partial \boldsymbol{u}_{\boldsymbol{t}}(\boldsymbol{x}, t)}{\partial t} + \big(\boldsymbol{v}_{\boldsymbol{t}}(\boldsymbol{x}, t) \cdot \nabla_{\boldsymbol{t}}\big)\boldsymbol{u}_{\boldsymbol{t}}(\boldsymbol{x}, t), \quad (\boldsymbol{x}, t) \in \mathring{\mathscr{P}} \times \mathbb{R}_{>0}. \tag{1}$$

where the tangential gradient is given by $\nabla_{\boldsymbol{t}} \triangleq \begin{bmatrix}\partial/\partial x & \partial/\partial y\end{bmatrix}^\mathrm{T}$, $\boldsymbol{V}_\mathrm{s}(t) = \begin{bmatrix}V_{\mathrm{s}x}(t) & V_{\mathrm{s}y}(t)\end{bmatrix}^\mathrm{T}$ is the so-called *sliding velocity* of the contact patch centre, defined as

$$\boldsymbol{V}_\mathrm{s}(t) \triangleq \boldsymbol{V}_C(t) - \boldsymbol{V}_\mathrm{r}(t) = \begin{bmatrix}V_{Cx}(t) + \omega_y(t)R_\mathrm{r} \\ V_{Cy}(t) - \omega_x(t)R_\mathrm{r}\end{bmatrix}, \tag{2}$$

and the tensor $\mathbf{A}_{\omega_z}(t)$ reads

$$\mathbf{A}_{\omega_z}(t) = \begin{bmatrix} 0 & -\omega_z(t) \\ \omega_z(t) & 0 \end{bmatrix}, \tag{3}$$

in which $\omega_z(t) = \dot{\psi}(t) + \omega_\gamma(t)$ is the total angular speed of the rolling body around the vertical axis. The angular speeds $\dot{\psi}(t)$ and $\omega_\gamma(t)$ may be expressed as ratios of the total angular speed $\omega_\gamma(t) = \chi_\gamma(t)\omega_z(t)$ and $\dot{\psi}(t) = \chi_\psi(t)\omega_z(t)$, where $\chi_\gamma(t)$ and $\chi_\psi(t)$ are called *tilt* and *turn* ratio, respectively, and satisfy $\chi_\gamma(t) + \chi_\psi(t) = 1$ for all $t$.

Equation (1) is very general and valid for any $\boldsymbol{x}$ in $\mathscr{P}$. However, depending on the values of the micro-sliding velocity, two other relationships need to be considered:

$$\boldsymbol{v}_{\mathrm{s}}(\boldsymbol{x}, s) = \mathbf{0} \implies q_{\boldsymbol{t}}(\boldsymbol{x}, s) \leq \mu q_z(\boldsymbol{x}), \tag{4a}$$

$$\boldsymbol{v}_{\mathrm{s}}(\boldsymbol{x}, s) \neq \mathbf{0} \iff \boldsymbol{q}_{\boldsymbol{t}}(\boldsymbol{x}, s) = -\mu q_z(\boldsymbol{x}) \frac{\boldsymbol{v}_{\mathrm{s}}(\boldsymbol{x}, s)}{v_{\mathrm{s}}(\boldsymbol{x}, s)}. \tag{4b}$$

In Eqs. (4), $q_{\boldsymbol{t}}(\boldsymbol{x}, s) = \big\|\boldsymbol{q}_{\boldsymbol{t}}(\boldsymbol{x}, s)\big\|$, $v_{\mathrm{s}}(\boldsymbol{x}, s) = \big\|\boldsymbol{v}_{\mathrm{s}}(\boldsymbol{x}, s)\big\|$, the symbol $q_z(\boldsymbol{x}, t)$ denotes the vertical pressure distribution acting inside the contact patch, and $\mu$ is the friction coefficient. Specifically, this paper assumes a constant value for $\mu$, according to the Amontons-Coulomb formulation, whereas more realistic models also account for its dependence on several parameters, like, e.g., temperature and local micro-sliding velocity [43–48]. The available friction $\mu q_z(\boldsymbol{x}, t)$ is finally known in the literature as *the traction bound*, since it limits the value of the shear stress acting upon the bristles.

Equations (4a) and (4b) define the adhesion and sliding zones $\mathscr{P}^{(\mathrm{a})}$, $\mathscr{P}^{(\mathrm{s})}$ of the contact patch:

$$\mathscr{P}^{(\mathrm{a})} \triangleq \big\{\boldsymbol{x} \in \mathscr{P} \;\big|\; \text{Eq. (4a) holds}\big\}, \tag{5a}$$

$$\mathscr{P}^{(\mathrm{s})} \triangleq \big\{\boldsymbol{x} \in \mathscr{P} \;\big|\; \text{Eq. (4b) holds}\big\}. \tag{5b}$$

In the following, keeping the notation used for $\mathscr{P}^{(\mathrm{a})}$ and $\mathscr{P}^{(\mathrm{s})}$, the superscripts $(\cdot)^{(\mathrm{a})}(\boldsymbol{x})$ and $(\cdot)^{(\mathrm{s})}(\boldsymbol{x})$ indicate that a physical quantity belongs to the adhesion and sliding regions of the contact patch $\mathscr{P}$, respectively.

## 2.1 Boundary and initial conditions

Equation (1) may be uniquely solved by enforcing an appropriate boundary condition (BC) and an initial condition (IC). In particular, the notion of BC for the problem under consideration strictly relates to those of *leading edge* $\mathscr{L}$, *neutral edge* $\mathscr{N}$ and *trailing edge* $\mathscr{T}$. The following Definition 2.1 is reminiscent of the recent works by Romano et al. [39].

**Definition 2.1** (Leading edge, neutral edge and trailing edge)**.** *The leading, neutral and trailing edges* $\mathscr{L}$, $\mathscr{N}$ *and* $\mathscr{T}$ *are defined respectively by*

$$\mathscr{L} \triangleq \left\{\boldsymbol{x} \in \partial\mathscr{P} \;\middle|\; \big[\boldsymbol{v}_{\boldsymbol{t}}(\boldsymbol{x}, t) - \boldsymbol{v}_{\partial\mathscr{P}}(\boldsymbol{x}, t)\big] \cdot \hat{\boldsymbol{\nu}}_{\partial\mathscr{P}}(\boldsymbol{x}, t) < 0\right\}, \tag{6a}$$

$$\mathscr{N} \triangleq \left\{\boldsymbol{x} \in \partial\mathscr{P} \;\middle|\; \big[\boldsymbol{v}_{\boldsymbol{t}}(\boldsymbol{x}, t) - \boldsymbol{v}_{\partial\mathscr{P}}(\boldsymbol{x}, t)\big] \cdot \hat{\boldsymbol{\nu}}_{\partial\mathscr{P}}(\boldsymbol{x}, t) = 0\right\}, \tag{6b}$$

$$\mathscr{T} \triangleq \left\{\boldsymbol{x} \in \partial\mathscr{P} \;\middle|\; \big[\boldsymbol{v}_{\boldsymbol{t}}(\boldsymbol{x}, t) - \boldsymbol{v}_{\partial\mathscr{P}}(\boldsymbol{x}, t)\big] \cdot \hat{\boldsymbol{\nu}}_{\partial\mathscr{P}}(\boldsymbol{x}, t) > 0\right\}. \tag{6c}$$

In Eqs. (6), the vector $\hat{\boldsymbol{\nu}}_{\partial\mathscr{P}}(\boldsymbol{x}, t)$ denotes the outward-pointing unit normal to $\partial\mathscr{P}$, and $\boldsymbol{v}_{\partial\mathscr{P}}(\boldsymbol{x}, t)$ is the velocity of the boundary of the contact patch $\partial\mathscr{P}$, and may be calculated as explained in Appendix A (it should be emphasised that, for a fixed contact patch, the term $\boldsymbol{v}_{\partial\mathscr{P}}(\boldsymbol{x}, t)$ vanishes, i.e. $\boldsymbol{v}_{\partial\mathscr{P}}(\boldsymbol{x}, t) = \mathbf{0}$). In this context, it is essential to clarify that, in this paper, the dynamics of the boundary $\partial\mathscr{P}$ of the contact patch is assumed not to be influenced by the bristle deflection $\boldsymbol{u}_{\boldsymbol{t}}(\boldsymbol{x}, s)$, as customarily done also by Kalker [49, 50].

The scalar product $\big[\boldsymbol{v}_{\boldsymbol{t}}(\boldsymbol{x}, t) - \boldsymbol{v}_{\partial\mathscr{P}}(\boldsymbol{x}, t)\big] \cdot \hat{\boldsymbol{\nu}}_{\partial\mathscr{P}}(\boldsymbol{x}, s)$ represents the flow of the bristles through the boundary $\partial\mathscr{P}$ of the contact patch, and, when negative, indicates that the bristles are entering $\mathscr{P}$. It is worth emphasising that Eqs. (6) presume the existence of the unit normal. For a rolling spherical wheel, this paper only considers a circular contact patch, according to Assumption 2.1, and therefore the unit normal to $\partial\mathscr{P}$ is always well-defined.

**Assumption 2.1** (Circular contact patch)**.** *The contact patch may be represented mathematically as*

$$\mathscr{P} \triangleq \Big\{ \boldsymbol{x} \in \Pi \;\Big|\; x^2 + y^2 \leq a^2(t) \Big\}, \tag{7}$$

*where $a(t)$ is the (possibly) time-varying contact patch radius.*

In any case, recalling Definition 2.1, the BC may formalised as

$$\text{BC:} \qquad \boldsymbol{u_t}(\boldsymbol{x}, t) = \boldsymbol{0}, \qquad (\boldsymbol{x}, t) \in \mathscr{L} \times \mathbb{R}_{>0}. \tag{8}$$

The physical interpretation of the BC (8) is that the bristles must be undeformed when entering the contact patch $\mathscr{P}$. On the other hand, the IC may be cast in mathematical form as follows:

$$\text{IC:} \qquad \boldsymbol{u_t}(\boldsymbol{x}, 0) = \boldsymbol{u_{t0}}(\boldsymbol{x}), \qquad \boldsymbol{x} \in \mathring{\mathscr{P}}_0, \tag{9}$$

for some[1] $\boldsymbol{u_{t0}} \in C^1(\mathring{\mathscr{P}}_0; \mathbb{R}^2)$, with $\boldsymbol{u_{t0}}(\boldsymbol{x}) = \boldsymbol{0}$ on $\mathscr{L}_0 \triangleq \mathscr{L}(0)$.

Similar BCs and ICs to those stated in Eqs. (8) and (9) may be also prescribed in the transition from adhesion to sliding and *vice versa*. In this respect, a more exhaustive discussion may be found in e.g. [39]. Instead, in the next Sects. 3, 4 and 5, closed-form expressions for the deflection of the bristle are derived under the assumption of vanishing sliding, that is $\mathscr{P}^{(\mathrm{a})} \equiv \mathscr{P}$. This allows to reformulate the governing PDEs (1) with $\boldsymbol{v}_{\mathrm{s}}(\boldsymbol{x}, t) = \boldsymbol{0}$ all over the contact patch. On the other hand, when the more stringent situation of limited friction is considered, the solutions deduced starting from vanishing sliding must be properly bounded considering the constraint given by Eq. (4a). In general, it is not possible to derive simple analytical representation for the sliding deflection $\boldsymbol{u}_{\boldsymbol{t}}^{(\mathrm{s})}(\boldsymbol{x}, t)$ in $\mathscr{P}^{(\mathrm{s})}$, whereas numerical techniques are required. This aspect is discussed in greater detail in Sect. 6 (and partially Sect. 5 for the singular case of a purely spinning sphere), which is dedicated to the calculation of the forces and moment acting on the spherical wheel.

# 3 Rolling spherical wheel

The first case analysed in this paper is that of a simply rolling spherical wheel, for which the velocity field $\boldsymbol{v_t}(\boldsymbol{x}, t)$ is given by

$$\boldsymbol{v_t}(\boldsymbol{x}, t) = \begin{bmatrix} \omega_y(t) \\ -\omega_x(t) \end{bmatrix} R_{\mathrm{r}}. \tag{10}$$

This type of kinematics is typical, for example, of triple and dual-axis rolling spherical robots [7] and conventional wheel with pneumatic tyres (with $\varepsilon_x = 0$ and $\varepsilon_y = 1$) subjected to relatively small camber angles and spin velocities. In these cases, the contribution of the term $\chi_\psi(t)\boldsymbol{u_t}(\boldsymbol{x}, t)$ in the right-hand side of Eq. (1) is negligible, and therefore will be disregarded in the following analysis.

Assuming $V_{\mathrm{r}}(t) \triangleq \big\|\boldsymbol{V}_{\mathrm{r}}(t)\big\| = \sqrt{\omega_x^2(t) + \omega_y^2(t)} R_{\mathrm{r}} > 0$ for all $t$, Eq. (1) with $\boldsymbol{v_t}(\boldsymbol{x}, t)$ as in Eq. (10) may be recast in nondimensional velocity form by defining the notion of travelled distance as $s \triangleq \int_0^t V_{\mathrm{r}}(t')\,\mathrm{d}t'$. Dividing Eq. (1) by $V_{\mathrm{r}}(t)$, setting $\boldsymbol{v}_{\mathrm{s}}(\boldsymbol{x}, t) = \boldsymbol{0}$, and approximating $\chi_\psi(t) \approx 0$ yields

$$\frac{\partial \boldsymbol{u_t}(\boldsymbol{x}, s)}{\partial s} + \big(\bar{\boldsymbol{v}}_{\boldsymbol{t}}(\boldsymbol{x}, s) \cdot \nabla_{\boldsymbol{t}}\big)\boldsymbol{u_t}(\boldsymbol{x}, s) = \boldsymbol{\sigma}(s) + \mathbf{A}_\varphi(s)\boldsymbol{x}, \qquad (\boldsymbol{x}, s) \in \mathring{\mathscr{P}} \times \mathbb{R}_{>0}, \tag{11}$$

where the following have been defined:

$$\boldsymbol{\sigma}(s) = \begin{bmatrix} \sigma_x(s) \\ \sigma_y(s) \end{bmatrix} \triangleq -\frac{\boldsymbol{V}_{\mathrm{s}}(s)}{V_{\mathrm{r}}(s)}, \tag{12a}$$

$$\boldsymbol{\varepsilon}(s) = \begin{bmatrix} \varepsilon_x(s) \\ \varepsilon_y(s) \end{bmatrix} \triangleq -\frac{R_{\mathrm{r}}}{V_{\mathrm{r}}(s)} \begin{bmatrix} \omega_x(s) \\ \omega_y(s) \end{bmatrix}, \tag{12b}$$

$$\mathbf{A}_\varphi(s) = \begin{bmatrix} 0 & -\varphi(s) \\ \varphi(s) & 0 \end{bmatrix} \triangleq -\frac{1}{V_{\mathrm{r}}(s)} \mathbf{A}_{\omega_z}(s). \tag{12c}$$

[1] As discussed extensively in [39], solutions of the type $\boldsymbol{u_t} \in C^1(\mathring{\mathscr{P}} \times \mathbb{R}_{>0})$ are not always possible according to the brush theory, and therefore it is not obvious that $\boldsymbol{u_{t0}} \in C^1(\mathring{\mathscr{P}}_0; \mathbb{R}^2)$ holds. When the initial conditions are only $C^0(\mathscr{P}_0)$, only weak solutions can be found.

In Eqs. (12), the quantities $\sigma_x(s)$ and $\sigma_y(s)$ are referred to as *longitudinal* and *lateral slip*. In respect to Eq. (12b), the vector $\boldsymbol{\varepsilon}(t)$ does not have any particular name, but it is worth noticing that $\left\|\boldsymbol{\varepsilon}(s)\right\| = 1$ for all $s$. Finally, the spin $\varphi(s)$ may further be decomposed as $\varphi(s) = \varphi_\gamma(s) + \varphi_\psi(s)$:

$$\varphi_\gamma(s) \triangleq -\frac{\omega_\gamma(s)}{V_\mathrm{r}(s)}, \tag{13a}$$

$$\varphi_\psi(s) \triangleq -\frac{\dot{\psi}(s)}{V_\mathrm{r}(s)}. \tag{13b}$$

The quantities $\varphi_\gamma(s)$ and $\varphi_\psi(s)$ are called in this paper *tilt* and *turn spin*, respectively. They may be interpreted as two different signed curvatures[2] $\varphi_\gamma = 1/R_\gamma$ and $\varphi_\psi = -1/R_\psi$ [54]; the actual curvature of the contact patch centre is thus given by the difference $\varphi = 1/R_\gamma - 1/R_\psi$. It may be easily verified that it holds $\varphi_\gamma(s) = \chi_\gamma(s)\varphi(s)$ and $\varphi_\psi(s) = \chi_\psi(s)\varphi(s)$.

Combining Eq. (10) with (12b), the nondimensional velocity field $\bar{\boldsymbol{v}}_{\boldsymbol{t}}(\boldsymbol{x}, s)$ in Eq. (11) may also be deduced reading

$$\bar{\boldsymbol{v}}_{\boldsymbol{t}}(\boldsymbol{x}, s) = -\begin{bmatrix} \varepsilon_y(s) \\ -\varepsilon_x(s) \end{bmatrix}. \tag{14}$$

Owing to these premises, the complete solution to Eq. (11), equipped with BC (8) and IC (9)[3], may be easily derived according to the well-established theory for linear PDEs [51, 52]. In particular, a parametrisation of the type $\boldsymbol{x} = \boldsymbol{x}(\boldsymbol{\rho}, \varsigma)$, $s = s(\boldsymbol{\rho}, \varsigma)$, $\boldsymbol{u}_{\boldsymbol{t}}(\boldsymbol{x}, s) = \boldsymbol{u}_{\boldsymbol{t}}(\boldsymbol{x}(\boldsymbol{\rho}, \varsigma), s(\boldsymbol{\rho}, \varsigma)) = \boldsymbol{\zeta}(\boldsymbol{\rho}, \varsigma)$ turns Eq. (11) into the following system of ODEs:

$$\frac{\mathrm{d}s(\boldsymbol{\rho}, \varsigma)}{\mathrm{d}\varsigma} = 1, \tag{15a}$$

$$\frac{\mathrm{d}\boldsymbol{x}(\boldsymbol{\rho}, \varsigma)}{\mathrm{d}\varsigma} = -\begin{bmatrix} \varepsilon_y(s) \\ -\varepsilon_x(s) \end{bmatrix}, \tag{15b}$$

$$\frac{\mathrm{d}\boldsymbol{\zeta}(\boldsymbol{\rho}, \varsigma)}{\mathrm{d}\varsigma} = \boldsymbol{\sigma}(s) + \mathbf{A}_\varphi(s)\boldsymbol{x}(\boldsymbol{\rho}, \varsigma), \tag{15c}$$

whose solution reads

$$s(\boldsymbol{\rho}, \varsigma) = \varsigma + s_0(\boldsymbol{\rho}), \tag{16a}$$

$$\boldsymbol{x}(\boldsymbol{\rho}, \varsigma) = \boldsymbol{x}_0(\boldsymbol{\rho}) - \int_0^\varsigma \begin{bmatrix} \varepsilon_y\big(\varsigma' + s_0(\boldsymbol{\rho})\big) \\ -\varepsilon_x\big(\varsigma' + s_0(\boldsymbol{\rho})\big) \end{bmatrix} \mathrm{d}\varsigma', \tag{16b}$$

$$\boldsymbol{\zeta}(\boldsymbol{\rho}, \varsigma) = \boldsymbol{\zeta}_0(\boldsymbol{\rho}) + \int_0^\varsigma \boldsymbol{\sigma}\big(\varsigma' + s_0(\boldsymbol{\rho})\big) + \mathbf{A}_\varphi\big(\varsigma' + s_0(\boldsymbol{\rho})\big)\boldsymbol{x}\big(\boldsymbol{\rho}, \varsigma'\big)\, \mathrm{d}\varsigma'. \tag{16c}$$

Starting from the above Eqs. (16), an analytical expression for the original variable $\boldsymbol{u}_{\boldsymbol{t}}(\boldsymbol{x}, s) = \boldsymbol{\zeta}(\boldsymbol{\rho}(\boldsymbol{x}, s), \varsigma(\boldsymbol{x}, s))$ may be derived by finding the inverse mapping between the coordinates $(\boldsymbol{\rho}, \varsigma)$ and $(\boldsymbol{x}, s)$. This mapping is unique provided that the boundary and initial conditions are *noncharacteristic* [51, 52]. The noncharacteristic requirement makes it possible to find a $C^2$ function solving the PDEs (11) in the proximity of the boundary (or initial) curve [51]. A similar argument also constitutes the basis for the Cauchy-Kovalevskaya existence and uniqueness theorem. For the problem under consideration, it has been proved in [39] that the BC (8) and IC (9), respectively, are always noncharacteristic. For many cases of interest, analogous conclusions about the well-posedness of the brush models under vanishing sliding conditions may be drawn as an application of the energy method (Appendix B). In the transient brush theory, however, functions solving (11) are usually only $C^0$ due to the possible non-analiticity of the initial conditions (for example when $\boldsymbol{u}_{\boldsymbol{t}0}(\boldsymbol{x})$ is only $C^0(\mathscr{P}_0)$). In these cases, only weak solutions may be found even under vanishing sliding conditions.

In any case, prescribing the BC (8) or IC (9) in turn provides two different solutions $\boldsymbol{u}_{\boldsymbol{t}}^-(\boldsymbol{x}, s)$ and $\boldsymbol{u}_{\boldsymbol{t}}^+(\boldsymbol{x}, s)$, which should be interpreted as a stationary (or steady-state) and transient one, respectively. The general procedure to recover them is illustrated in detail in Sects. 3.1 and 3.2.

[2] The convention for the sign for the radii $R_\gamma$ and $R_\psi$ is adopted from the discipline of Vehicle Dynamics.

[3] Clearly with the time variable $t$ replaced by the travelled distance $s$.

### 3.1 Steady-state solution

The steady-state solution for the bristle deflection may be easily recovered when all the involved quantities are constant over travelled distance. In this case, the integral solutions given by Eqs. (16) simplify to

$$s(\boldsymbol{\rho}, \varsigma) = \varsigma + s_0(\boldsymbol{\rho}), \tag{17a}$$

$$\boldsymbol{x}(\boldsymbol{\rho}, \varsigma) = \boldsymbol{x}_0(\boldsymbol{\rho}) - \begin{bmatrix} \varepsilon_y \\ -\varepsilon_x \end{bmatrix} \varsigma, \tag{17b}$$

$$\boldsymbol{\zeta}(\boldsymbol{\rho}, \varsigma) = \boldsymbol{\zeta}_0(\boldsymbol{\rho}) + \boldsymbol{\sigma}\varsigma + \mathbf{A}_\varphi \varsigma \left( \boldsymbol{x}_0(\boldsymbol{\rho}) - \begin{bmatrix} \varepsilon_y \\ -\varepsilon_x \end{bmatrix} \frac{\varsigma}{2} \right). \tag{17c}$$

To this end, it may be noticed that the BC (8) prescribes $\boldsymbol{\zeta}_0(\boldsymbol{\rho}) = \mathbf{0}$ on the leading edge. Moreover, Eq. (17b) may be manipulated further yielding

$$\varepsilon_x x + \varepsilon_y y = \varepsilon_x x_0(\boldsymbol{\rho}) + \varepsilon_y y_0(\boldsymbol{\rho}), \tag{18a}$$

$$\varsigma = \left\| \boldsymbol{x} - \boldsymbol{x}_0(\boldsymbol{\rho}) \right\|, \tag{18b}$$

which provide two relationships between the original set of variables $(\boldsymbol{x}, s)$ and the parametric coordinates $(\boldsymbol{\rho}, \varsigma)$. In particular, Eq. (18a) describes the trajectories of the roots of the bristles (i.e. the characteristic projections) travelling inside the contact patch. It may be easily inferred from Eq. (18a) that these correspond to straight lines parallel to the nondimensional velocity field, and departing from the leading edge. On the other hand, Eq. (18b) relates $\varsigma$ to the physical variables $\boldsymbol{x}$ and the initial coordinates $\boldsymbol{x}_0(\boldsymbol{\rho})$, expressed as a function of the parameters $\boldsymbol{\rho}$.

The relationships (18) may be inverted locally yielding an explicit solution for $\boldsymbol{u}_{\boldsymbol{t}}^-(\boldsymbol{x}, s)$ in the steady-state region of the contact patch $\mathscr{P}^-$. When $\mathscr{P}$ is fixed, this may always be done by choosing a parametrisation of the type $s_0(\boldsymbol{\rho}) = \rho_1$ and $\boldsymbol{x}_0(\boldsymbol{\rho}) = \boldsymbol{x}_0(\rho_2)$. In this context, the cases when either $\varepsilon_x = 0$ or $\varepsilon_y = 0$ admit respectively explicit representations of the leading edge in the form

$$x = x_{\mathscr{L}}(y) = \varepsilon_y \sqrt{a^2 - y^2}, \qquad y \in (-a, a), \tag{19a}$$

$$y = y_{\mathscr{L}}(x) = -\varepsilon_x \sqrt{a^2 - x^2}, \qquad x \in (-a, a). \tag{19b}$$

Therefore, setting, in turn, $y(\rho_2) = \rho_2$ and $x(\rho_2) = \rho_2$, the following expressions may be derived for the initial coordinates $\boldsymbol{x}_0(\boldsymbol{\rho}(\boldsymbol{x}))$ as a function of the physical variables $\boldsymbol{x}$:

$$y_0\big(\rho_2(\boldsymbol{x})\big) = y \qquad \text{and} \qquad x_0\big(\rho_2(\boldsymbol{x})\big) = \varepsilon_y \sqrt{a^2 - y^2}, \tag{20a}$$

$$x_0\big(\rho_2(\boldsymbol{x})\big) = x \qquad \text{and} \qquad y_0\big(\rho_2(\boldsymbol{x})\big) = -\varepsilon_x \sqrt{a^2 - x^2}. \tag{20b}$$

In contrast, when $\varepsilon_x \neq 0$, $\varepsilon_y \neq 0$, an analytical expression for $y_0\big(\rho_2(\boldsymbol{x})\big)$ may be deduced as

$$y_0\big(\rho_2(\boldsymbol{x})\big) = \varepsilon_y \Gamma(\boldsymbol{x}) - \varepsilon_x \sqrt{a^2 - \Gamma^2(\boldsymbol{x})}, \tag{21}$$

with

$$\Gamma(\boldsymbol{x}) \triangleq \varepsilon_x x + \varepsilon_y y. \tag{22}$$

The initial condition $x_0(\rho_2(\boldsymbol{x}))$ may be then derived by composition of $x_0(\rho_2(\boldsymbol{x})) = x_{\mathscr{L}_i} \circ y_0(\rho_2(\boldsymbol{x}))$, where $x_{\mathscr{L}_i}(\cdot)$ is again an explicit representation of the leading edge. In this context, some possible expressions for the parametrisation of the leading edge for different combinations of values of $\varepsilon_x$, $\varepsilon_y$ are reported in Appendix C (Eqs. (78), (79), (80) or (81)).

Combining Eq. (17c) with Eqs. (20) or alternatively Eqs. (21) and (22) and transforming back $\boldsymbol{u}_{\boldsymbol{t}}^-(\boldsymbol{x}, s) = \boldsymbol{\zeta}(\boldsymbol{\rho}(\boldsymbol{x}, s), \varsigma(\boldsymbol{x}, s))$ yields the final expression for deflection of the bristle inside the steady-state region of the contact patch:

$$\boldsymbol{u}_{\boldsymbol{t}}^-(\boldsymbol{x}) = \boldsymbol{\sigma}\Sigma(\boldsymbol{x}) + \mathbf{A}_\varphi \Sigma(\boldsymbol{x}) \left( \boldsymbol{x}_0\big(\rho_2(\boldsymbol{x})\big) - \begin{bmatrix} \varepsilon_y \\ -\varepsilon_x \end{bmatrix} \frac{\Sigma(\boldsymbol{x})}{2} \right), \qquad (\boldsymbol{x}, s) \in \mathscr{P}^- \times \mathbb{R}_{\geq 0} \tag{23}$$

where $\Sigma(\boldsymbol{x}) \triangleq \left\| \boldsymbol{x} - \boldsymbol{x}_0(\rho_2(\boldsymbol{x})) \right\|$. In Eq. (23), the domain $\mathscr{P}^-$ may be defined from the condition $s_0(\rho_1(\boldsymbol{x}, s)) = \rho_1(\boldsymbol{x}, s) > 0$, which implies $s > \Sigma(\boldsymbol{x})$. Thus, introducing

$$\gamma_\Sigma(\boldsymbol{x}, s) \triangleq \Sigma(\boldsymbol{x}) - s, \tag{24}$$

it is possible to define $\mathscr{P}^-$ mathematically as follows:

$$\mathscr{P}^- \triangleq \big\{\boldsymbol{x} \in \mathscr{P} \;\big|\; \gamma_\Sigma(\boldsymbol{x}, s) < 0\big\}, \tag{25}$$

since the implicit curve $\gamma_\Sigma(\boldsymbol{x}, s) = 0$ separates the steady-state domain from the transient one. Therefore, the curve described by $\gamma_\Sigma(\boldsymbol{x}, s) = 0$ is referred to as *transient* or *travelling edge* [39].

It is important to remark that, owing to the assumption of constant slips and velocities, the expression for $\boldsymbol{u}_{\boldsymbol{t}}^-(\boldsymbol{x})$ in Eq. (23) does not depend on the variable $s$, and therefore is actually steady-state. For variable slip inputs, in contrast, the solution sought by imposing the BC (8) would still have been *stationary*, but also time-varying.

### 3.2 Transient solution

The transient solution $\boldsymbol{u}_{\boldsymbol{t}}^+(\boldsymbol{x}, s)$ may be obtained by parametrising $\boldsymbol{x}_0(\boldsymbol{\rho}) = \boldsymbol{\rho}$ for $s_0(\boldsymbol{\rho}) = 0$. It follows from compatibility that $\boldsymbol{\zeta}_0(\boldsymbol{\rho}(\boldsymbol{x}, s)) = \boldsymbol{u}_{\boldsymbol{t}0}(\boldsymbol{x}_0(\boldsymbol{x}, s))$, and therefore the transient solution is given by

$$\boldsymbol{u}_{\boldsymbol{t}}^+(\boldsymbol{x}, s) = \boldsymbol{u}_{\boldsymbol{t}0}\big(\boldsymbol{x}_0(\boldsymbol{x}, s)\big) + \int_0^s \boldsymbol{\sigma}\big(s'\big) + \mathbf{A}_\varphi\big(s'\big)\boldsymbol{x}\big(\boldsymbol{\rho}, s'\big)\,\mathrm{d}s', \tag{26}$$

where $\boldsymbol{x}_0(\boldsymbol{x}, s)$ reads

$$\boldsymbol{x}_0(\boldsymbol{x}, s) = \boldsymbol{x} + \int_0^s \begin{bmatrix} \varepsilon_y\big(s'\big) \\ -\varepsilon_x\big(s'\big) \end{bmatrix} \mathrm{d}s'. \tag{27}$$

Equations (26) and (27) provide the most general, closed-form expression for the transient solution under vanishing sliding conditions for a pure rolling sphere. When the slip quantities are constant, the above relationship (26) further simplifies to

$$\boldsymbol{u}_{\boldsymbol{t}}^+(\boldsymbol{x}, s) = \boldsymbol{u}_{\boldsymbol{t}0}\big(\boldsymbol{x}_0(\boldsymbol{x}, s)\big) + \boldsymbol{\sigma} s + \mathbf{A}_\varphi s\left(\boldsymbol{x}_0(\boldsymbol{x}, s) - \begin{bmatrix} \varepsilon_y \\ -\varepsilon_x \end{bmatrix} \frac{s}{2}\right), \qquad (\boldsymbol{x}, s) \in \mathscr{P}^+ \times \mathbb{R}_{\geq 0}, \tag{28}$$

where $\boldsymbol{x}_0(\boldsymbol{x}, s) = \boldsymbol{x} + \begin{bmatrix} \varepsilon_y & -\varepsilon_x \end{bmatrix}^{\mathrm{T}} s$. In this case, the transient solution applies in the transient region of the contact patch defined by [39]

$$\mathscr{P}^+ \triangleq \big\{\boldsymbol{x} \in \mathscr{P} \;\big|\; \gamma_\Sigma(\boldsymbol{x}, s) \geq 0\big\}, \tag{29}$$

and is clearly continuous on the travelling edge, that is $\boldsymbol{u}_{\boldsymbol{t}}^+(\boldsymbol{x}, \Sigma(\boldsymbol{x})) \equiv \boldsymbol{u}_{\boldsymbol{t}}^-(\boldsymbol{x})$. The global solution over the contact patch $\mathscr{P} = \mathscr{P}^- \cup \mathscr{P}^+$ may be then formally constructed as

$$\boldsymbol{u}_{\boldsymbol{t}}(\boldsymbol{x}, s) = \begin{cases} \boldsymbol{u}_{\boldsymbol{t}}^-(\boldsymbol{x}), & (\boldsymbol{x}, s) \in \mathscr{P}^- \times \mathbb{R}_{\geq 0}, \\ \boldsymbol{u}_{\boldsymbol{t}}^+(\boldsymbol{x}, s), & (\boldsymbol{x}, s) \in \mathscr{P}^+ \times \mathbb{R}_{\geq 0}. \end{cases} \tag{30}$$

As opposed to the steady-state solution, the transient deflection of the bristle $\boldsymbol{u}_{\boldsymbol{t}}^+(\boldsymbol{x}, s)$ in Eq. (28) does not require an explicit parametrisation of the leading edge, and therefore is formally independent of the shape of the contact patch. On the other hand, it depends on the travelled distance $s$.

## 4 Rolling and tilting spherical wheel

For a rolling and tilting spherical wheel, the velocity field reads

$$\boldsymbol{v}_{\boldsymbol{t}}(\boldsymbol{x}, t) = \begin{bmatrix} \omega_y(t) \\ -\omega_x(t) \end{bmatrix} R_{\mathrm{r}} - \mathbf{A}_{\omega_\gamma}(t)\boldsymbol{x}, \tag{31}$$

being $\mathbf{A}_{\omega_\gamma}(t) \triangleq -\chi_\gamma(t)\mathbf{A}_{\omega_z}(t)$. The kinematic described by Eq. (31) is typical of rolling and steering spherical robots [7], or wheel with tyres subjected to large camber angles (again with $\varepsilon_x = 0$ and $\varepsilon_y = 1$, when small contributions to the lateral speed due to variations in the tilt angle are disregarded).

With the same transformation $s \triangleq \int_0^t V_{\mathrm{r}}(t')\,\mathrm{d}t'$ of Sect. 3, and enforcing $\boldsymbol{v}_{\mathrm{s}}(\boldsymbol{x}, t) = \mathbf{0}$, Eq. (1) becomes

$$\frac{\partial \boldsymbol{u}_{\boldsymbol{t}}(\boldsymbol{x}, s)}{\partial s} + \big(\bar{\boldsymbol{v}}_{\boldsymbol{t}}(\boldsymbol{x}, s) \cdot \nabla_{\boldsymbol{t}}\big)\boldsymbol{u}_{\boldsymbol{t}}(\boldsymbol{x}, s) = \boldsymbol{\sigma}(s) + \mathbf{A}_\varphi(s)\big(\boldsymbol{x} + \chi_\psi(s)\boldsymbol{u}_{\boldsymbol{t}}(\boldsymbol{x}, s)\big), \qquad (\boldsymbol{x}, s) \in \mathring{\mathscr{P}} \times \mathbb{R}_{>0}, \tag{32}$$

with $\boldsymbol{\sigma}(s)$ and $\mathbf{A}_{\varphi}(s)$ defined as in Eqs. (12), the nondimensional velocity field $\bar{\boldsymbol{v}}_{\boldsymbol{t}}(\boldsymbol{x}, s)$ reading

$$\bar{\boldsymbol{v}}_{\boldsymbol{t}}(\boldsymbol{x}, s) = -\begin{bmatrix} \varepsilon_y(s) \\ -\varepsilon_x(s) \end{bmatrix} + \mathbf{A}_{\varphi_\gamma}(s)\boldsymbol{x}, \tag{33}$$

and

$$\mathbf{A}_{\varphi_\gamma}(s) = \begin{bmatrix} 0 & \varphi_\gamma(s) \\ -\varphi_\gamma(s) & 0 \end{bmatrix} \triangleq -\frac{1}{V_{\mathrm{r}}(s)}\mathbf{A}_{\omega_\gamma}(s). \tag{34}$$

It should be observed that the BC and IC for the transformed PDEs (32) are given again by (8) and IC (9).

In this case, assuming a similar parametrisation to that in Sect. (3), the original PDEs (32) are converted into

$$\frac{\mathrm{d}s(\boldsymbol{\rho}, \varsigma)}{\mathrm{d}\varsigma} = 1, \tag{35a}$$

$$\frac{\mathrm{d}\boldsymbol{x}(\boldsymbol{\rho}, \varsigma)}{\mathrm{d}\varsigma} = \mathbf{A}_{\varphi_\gamma}(s)\big(\boldsymbol{x}(\boldsymbol{\rho}, \varsigma) - \boldsymbol{x}_{C_\gamma}(s)\big), \tag{35b}$$

$$\frac{\mathrm{d}\boldsymbol{\zeta}(\boldsymbol{\rho}, \varsigma)}{\mathrm{d}\varsigma} = \mathbf{A}_{\varphi_\psi}(s)\boldsymbol{\zeta}(\boldsymbol{\rho}, \varsigma) + \boldsymbol{\sigma}(s) + \mathbf{A}_{\varphi}(s)\boldsymbol{x}(\boldsymbol{\rho}, \varsigma), \tag{35c}$$

in which the *turning tensor* reads $\mathbf{A}_{\varphi_\psi}(s) = \chi_\psi(s)\mathbf{A}_{\varphi}(s)$. The quantity

$$\boldsymbol{x}_{C_\gamma}(s) = \begin{bmatrix} x_{C_\gamma}(s) & y_{C_\gamma}(s) \end{bmatrix}^{\mathrm{T}} \triangleq \begin{bmatrix} \varepsilon_x(s)/\varphi_\gamma(s) & \varepsilon_y(s)/\varphi_\gamma(s) \end{bmatrix}^{\mathrm{T}} \tag{36}$$

should be regarded as *instantaneous tilting centre*, meaning that, freezing the time for a fixed value of travelled distance $s$, the trajectories of the bristles travelling inside the contact patch might be interpreted as circular ones centred in $\boldsymbol{x}_{C_\gamma}(s)$.

The integral solution for the system above may be recovered from its Peano-Baker series as follows [39, 55, 56]:

$$s(\boldsymbol{\rho}, \varsigma) = \varsigma + s_0(\boldsymbol{\rho}), \tag{37a}$$

$$\boldsymbol{x}(\boldsymbol{\rho}, \varsigma) = \boldsymbol{\Phi}_{\varphi_\gamma}(\varsigma, 0)\boldsymbol{x}_0(\boldsymbol{\rho}) - \int_0^{\varsigma} \boldsymbol{\Phi}_{\varphi_\gamma}\big(\varsigma, \varsigma'\big)\mathbf{A}_{\varphi_\gamma}\big(\varsigma' + s_0(\boldsymbol{\rho})\big)\boldsymbol{x}_{C_\gamma}\big(\varsigma' + s_0(\boldsymbol{\rho})\big)\,\mathrm{d}\varsigma', \tag{37b}$$

$$\boldsymbol{\zeta}(\boldsymbol{\rho}, \varsigma) = \boldsymbol{\Phi}_{\varphi_\psi}(\varsigma, 0)\boldsymbol{\zeta}_0(\boldsymbol{\rho}) + \int_0^{\varsigma} \boldsymbol{\Phi}_{\varphi_\psi}\big(\varsigma, \varsigma'\big)\Big[\boldsymbol{\sigma}\big(\varsigma' + s_0(\boldsymbol{\rho})\big) + \mathbf{A}_{\varphi}\big(\varsigma' + s_0(\boldsymbol{\rho})\big)\boldsymbol{x}\big(\boldsymbol{\rho}, \varsigma'\big)\Big]\,\mathrm{d}\varsigma', \tag{37c}$$

where the generic transition matrices $\boldsymbol{\Phi}_{\varphi_\gamma}(\varsigma, \tilde{\varsigma})$ and $\boldsymbol{\Phi}_{\varphi_\psi}(\varsigma, \tilde{\varsigma})$ for the camber and turn spin read [39, 55]:

$$\boldsymbol{\Phi}_{\varphi_\gamma}(\varsigma, \tilde{\varsigma}) = \mathrm{e}^{\int_{\tilde{\varsigma}}^{\varsigma} \mathbf{A}_{\varphi_\gamma}(\varsigma' + s_0(\boldsymbol{\rho}))\,\mathrm{d}\varsigma'} = \begin{bmatrix} \cos\Big(\int_{\tilde{\varsigma}}^{\varsigma} \varphi_\gamma\big(\varsigma' + s_0(\boldsymbol{\rho})\big)\,\mathrm{d}\varsigma'\Big) & \sin\Big(\int_{\tilde{\varsigma}}^{\varsigma} \varphi_\gamma\big(\varsigma' + s_0(\boldsymbol{\rho})\big)\,\mathrm{d}\varsigma'\Big) \\ -\sin\Big(\int_{\tilde{\varsigma}}^{\varsigma} \varphi_\gamma\big(\varsigma' + s_0(\boldsymbol{\rho})\big)\,\mathrm{d}\varsigma'\Big) & \cos\Big(\int_{\tilde{\varsigma}}^{\varsigma} \varphi_\gamma\big(\varsigma' + s_0(\boldsymbol{\rho})\big)\,\mathrm{d}\varsigma'\Big) \end{bmatrix}, \tag{38a}$$

$$\boldsymbol{\Phi}_{\varphi_\psi}(\varsigma, \tilde{\varsigma}) = \mathrm{e}^{\int_{\tilde{\varsigma}}^{\varsigma} \mathbf{A}_{\varphi_\psi}(\varsigma' + s_0(\boldsymbol{\rho}))\,\mathrm{d}\varsigma'} = \begin{bmatrix} \cos\Big(\int_{\tilde{\varsigma}}^{\varsigma} \varphi_\psi\big(\varsigma' + s_0(\boldsymbol{\rho})\big)\,\mathrm{d}\varsigma'\Big) & -\sin\Big(\int_{\tilde{\varsigma}}^{\varsigma} \varphi_\psi\big(\varsigma' + s_0(\boldsymbol{\rho})\big)\,\mathrm{d}\varsigma'\Big) \\ \sin\Big(\int_{\tilde{\varsigma}}^{\varsigma} \varphi_\psi\big(\varsigma' + s_0(\boldsymbol{\rho})\big)\,\mathrm{d}\varsigma'\Big) & \cos\Big(\int_{\tilde{\varsigma}}^{\varsigma} \varphi_\psi\big(\varsigma' + s_0(\boldsymbol{\rho})\big)\,\mathrm{d}\varsigma'\Big) \end{bmatrix}. \tag{38b}$$

Considerations about the well-posedness of the problem are analogous to those already discussed in Sect. 3. Hence, the next Sects. 4.1 and 4.2 provide the solutions for the steady-state and transient deflections of the bristle, namely $\boldsymbol{u}_{\boldsymbol{t}}^{-}(\boldsymbol{x}, s)$ and $\boldsymbol{u}_{\boldsymbol{t}}^{+}(\boldsymbol{x}, s)$.

## 4.1 Steady-state solution

Similarly for the case of a rolling sphere illustrated in Sect. 3, closed-form expressions for the steady-state deflection of the bristle may be derived when the slip inputs and rolling velocities are constant over travelled distance. Moreover, the following analysis considers sufficiently small tilting angles, according to the following Assumption 4.1.

**Assumption 4.1** (Assumption on tilting radius)**.** *In absolute value, the tilting radius is greater than or equal to the contact patch radius, i.e.* $\big|R_\gamma\big| = 1/\big|\varphi_\gamma\big| \geq a$.

The importance of Assumption 4.1 will be clarified later on in this section. On the other hand, the condition on constant slips and spins simplifies the integral solution in Eqs. (37) as

$$s(\boldsymbol{\rho},\varsigma) = \varsigma + s_0(\boldsymbol{\rho}), \tag{39a}$$
$$\boldsymbol{x}(\boldsymbol{\rho},\varsigma) = \mathbf{R}_{\varphi_\gamma}(\varsigma)\big(\boldsymbol{x}_0(\boldsymbol{\rho}) - \boldsymbol{x}_{C_\gamma}\big) + \boldsymbol{x}_{C_\gamma}, \tag{39b}$$
$$\boldsymbol{\zeta}(\boldsymbol{\rho},\varsigma) = \mathbf{R}_{\varphi_\psi}(\varsigma)\Big(\boldsymbol{\zeta}_0(\boldsymbol{\rho}) - \tilde{\boldsymbol{\zeta}}_0(\boldsymbol{\rho})\Big) + \tilde{\boldsymbol{\zeta}}(\boldsymbol{\rho},\varsigma), \tag{39c}$$

where the *tilting* and *turning rotation matrices* $\mathbf{R}_{\varphi_\gamma}(\varsigma)$ and $\mathbf{R}_{\varphi_\psi}(\varsigma)$ are defined respectively as

$$\mathbf{R}_{\varphi_\gamma}(\varsigma) \triangleq \mathrm{e}^{\mathbf{A}_{\varphi_\gamma}\varsigma} = \begin{bmatrix} \cos(\varphi_\gamma\varsigma) & \sin(\varphi_\gamma\varsigma) \\ -\sin(\varphi_\gamma\varsigma) & \cos(\varphi_\gamma\varsigma) \end{bmatrix}, \tag{40a}$$
$$\mathbf{R}_{\varphi_\psi}(\varsigma) \triangleq \mathrm{e}^{\mathbf{A}_{\varphi_\psi}\varsigma} = \begin{bmatrix} \cos(\varphi_\psi\varsigma) & -\sin(\varphi_\psi\varsigma) \\ \sin(\varphi_\psi\varsigma) & \cos(\varphi_\psi\varsigma) \end{bmatrix}. \tag{40b}$$

and the coordinate vector $\boldsymbol{x}_{C_\gamma}$ becomes constant over travelled distance. In this case, it indicates the fixed position of the *tilting centre* $C_\gamma$ seen from the contact point. The function $\tilde{\boldsymbol{\zeta}}(\cdot,\cdot)$ reads

$$\tilde{\boldsymbol{\zeta}}(\boldsymbol{\rho},\varsigma) = -\mathbf{A}_{\varphi_\psi}^{-1}\boldsymbol{\sigma} - \boldsymbol{x}(\boldsymbol{\rho},\varsigma) + \boldsymbol{x}_{C_\psi}, \tag{41}$$

where the coordinate vector $\boldsymbol{x}_{C_\psi}$ denotes the position of the *turning centre*

$$\boldsymbol{x}_{C_\psi} = \begin{bmatrix} x_{C_\psi} & y_{C_\psi} \end{bmatrix}^{\mathrm{T}} \triangleq \begin{bmatrix} -\varepsilon_x/\varphi_\psi & -\varepsilon_y/\varphi_\psi \end{bmatrix}^{\mathrm{T}}. \tag{42}$$

Also in this case, the steady-state solution for the bristle deflection can be recovered with a similar procedure to that explained in Sect. 3. To this end, it may be first observed that $\tilde{\boldsymbol{\zeta}}(\boldsymbol{\rho},\varsigma)$ in Eq. (39) may be recast as $\tilde{\boldsymbol{\zeta}}(\boldsymbol{\rho}(\boldsymbol{x},s),\varsigma(\boldsymbol{x},s)) = \tilde{\boldsymbol{u}}_{\boldsymbol{t}}(\boldsymbol{x})$, with

$$\tilde{\boldsymbol{u}}_{\boldsymbol{t}}(\boldsymbol{x}) \triangleq -\mathbf{A}_{\varphi_\psi}^{-1}\boldsymbol{\sigma} - \boldsymbol{x} + \boldsymbol{x}_{C_\psi}. \tag{43}$$

Additionally, this time Eqs. (39b) may be rearranged in the form

$$\big(x - \varepsilon_x/\varphi_\gamma\big)^2 + \big(y - \varepsilon_y/\varphi_\gamma\big)^2 = \big(x_0(\boldsymbol{\rho}) - \varepsilon_x/\varphi_\gamma\big)^2 + \big(y_0(\boldsymbol{\rho}) - \varepsilon_y/\varphi_\gamma\big)^2, \tag{44a}$$
$$\varsigma = \frac{1}{\varphi_\gamma}\left[\arctan\left(\frac{\varepsilon_y x - \varepsilon_x y}{\varepsilon_x x + \varepsilon_y y - 1/\varphi_\gamma}\right) - \arctan\left(\frac{\varepsilon_y x_0(\boldsymbol{\rho}) - \varepsilon_x y_0(\boldsymbol{\rho})}{\varepsilon_x x_0(\boldsymbol{\rho}) + \varepsilon_y y_0(\boldsymbol{\rho}) - 1/\varphi_\gamma}\right)\right], \tag{44b}$$

where Eq. (44a) indicates that the characteristic projections are circles intercepting the leading edge and centred in the tilting centre $C_\gamma$, and Eq. (44b) provides a mapping between the auxiliary variable $\varsigma$ and the space coordinates $\boldsymbol{x}$. In this context, it should be observed that, owing to Assumption 4.1, the relationship between $\varsigma$ and $\boldsymbol{x}$ in Eq. (44b) has been derived in a way such that the denominator of the arctan$(\cdot)$ functions does not vanish inside the interior $\mathring{\mathscr{P}}$ of the contact patch. In particular, the numerator of the arctan$(\cdot)$ functions represents a straight line from the centre of the contact patch to the cambering centre $C_\gamma$, whereas the denominator parametrises a line also passing through $C_\gamma$, but perpendicular to the former. It is also worth noticing that, for $\varepsilon_x = 0$ and $\varepsilon_y = 1$, the above Eq. (44b) simplifies to that obtained in [39] for a tyre.

Again, the expression for parametrisations of the initial coordinates in Eqs. (44) when either $\varepsilon_x$ or $\varepsilon_y$ vanishes become particularly simple. Specifically, for $\varepsilon_x = 0$, $\varepsilon_y = \pm 1$, the following parametrisations may be obtained

$$y_0\big(\rho_2(\boldsymbol{x})\big) = \frac{\varepsilon_y\varphi_\gamma\Lambda(\boldsymbol{x})}{2} \qquad \text{and} \qquad x_0\big(\rho_2(\boldsymbol{x})\big) = \varepsilon_y\sqrt{a^2 - \left(\frac{\varphi_\gamma\Lambda(\boldsymbol{x})}{2}\right)^2}. \tag{45}$$

Similarly, the combination $\varepsilon_x = \pm 1$, $\varepsilon_y = 0$ yields

$$x_0\big(\rho_2(\boldsymbol{x})\big) = \frac{\varepsilon_x\varphi_\gamma\Lambda(\boldsymbol{x})}{2} \qquad \text{and} \qquad y_0\big(\rho_2(\boldsymbol{x})\big) = -\varepsilon_x\sqrt{a^2 - \left(\frac{\varphi_\gamma\Lambda(\boldsymbol{x})}{2}\right)^2}. \tag{46}$$

In contrast, when both $\varepsilon_x$ and $\varepsilon_y$ are nonzero, a possible parametrisation of the initial condition $y_0(\boldsymbol{\rho}(\boldsymbol{x}))$ may be found in the form

$$y_0\big(\rho_2(\boldsymbol{x})\big) = \rho_2(\boldsymbol{x}) = \frac{\varepsilon_y\varphi_\gamma\Lambda(\boldsymbol{x})}{2} - \varepsilon_x\sqrt{a^2 - \left(\frac{\varphi_\gamma\Lambda(\boldsymbol{x})}{2}\right)^2}, \tag{47}$$

where this time

$$\Lambda(\boldsymbol{x}) = a^2 + \frac{1}{\varphi_\gamma^2} - \Gamma(\boldsymbol{x}), \tag{48a}$$

$$\Gamma(\boldsymbol{x}) = \big(x - \varepsilon_x/\varphi_\gamma\big)^2 + \big(y - \varepsilon_y/\varphi_\gamma\big)^2. \tag{48b}$$

The initial coordinate $x_0(\rho_2(\boldsymbol{x}))$ may be then derived as $x_0(\rho_2(\boldsymbol{x})) = x_{\mathscr{L}_i} \circ y_0(\rho_2(\boldsymbol{x}))$, where $x_{\mathscr{L}_i}(\cdot)$ is an explicit representation of the leading edge, as given for example in Eqs. (78), (79), (80) or (81).

In this context, a quick inspection of Eqs. (45), (46) and (47) reveals that the parametrisations for the initial coordinates are well defined for

$$-\frac{2a}{\big|\varphi_\gamma\big|} \leq \Lambda(\boldsymbol{x}) \leq \frac{2a}{\big|\varphi_\gamma\big|}, \tag{49}$$

which, recalling Eq. (48a), may be recast as

$$\left(a - \frac{1}{\big|\varphi_\gamma\big|}\right)^2 \leq \Gamma(\boldsymbol{x}) \leq \left(a + \frac{1}{\big|\varphi_\gamma\big|}\right)^2. \tag{50}$$

The above inequality states that the points of the contact patch for which steady-state conditions can hold are those comprised between two circles, centred in $C_\gamma$, of radius $R_1^2 = (a - 1/\big|\varphi_\gamma\big|)^2$ and $R_2^2 = (a + 1/\big|\varphi_\gamma\big|)^2$, respectively. Therefore, the requirement $1/\big|\varphi_\gamma\big| \geq a$ in Assumption 4.1 guarantees that the deflection of the bristle admits a steady-state solution for all the points in $\mathring{\mathscr{P}}$[4]. Conversely, for higher values of $\big|\varphi_\gamma\big|$, there exists a circle inside the contact patch whose interior points are never reached by the characteristic projections departing from the leading edge. For these points, no steady-state solution can be recovered. The situation is illustrated graphically in Fig. 2, where the domains of validity for the steady-state solution $\boldsymbol{u}_{\boldsymbol{t}}^-(\boldsymbol{x})$ for the deflection of the bristle are shown for two different cases $\big|R_\gamma\big| = 1/\big|\varphi_\gamma\big| < a$ and $\big|R_\gamma\big| = 1/\big|\varphi_\gamma\big| > a$, respectively.

Owing to Assumption 4.1, the steady-state deflection of the bristle in a region $\mathscr{P}^-$ of the contact patch may be calculated:

$$\boldsymbol{u}_{\boldsymbol{t}}^-(\boldsymbol{x}) = \mathbf{R}_{\varphi_\psi}\big(\Sigma(\boldsymbol{x})\big)\boldsymbol{\Psi}(\boldsymbol{x}) + \tilde{\boldsymbol{u}}_{\boldsymbol{t}}(\boldsymbol{x}), \qquad (\boldsymbol{x}, s) \in \mathscr{P}^- \times \mathbb{R}_{\geq 0}, \tag{51}$$

where the functions $\Sigma(\cdot)$ and $\boldsymbol{\Psi}(\cdot)$ have been introduced as

$$\Sigma(\boldsymbol{x}) \triangleq \frac{1}{\varphi_\gamma}\left[\arctan\left(\frac{\varepsilon_y x - \varepsilon_x y}{\varepsilon_x x + \varepsilon_y y - 1/\varphi_\gamma}\right) - \arctan\left(\frac{\varepsilon_y x_0\big(\rho_2(\boldsymbol{x})\big) - \varepsilon_x y_0\big(\rho_2(\boldsymbol{x})\big)}{\varepsilon_x x_0\big(\rho_2(\boldsymbol{x})\big) + \varepsilon_y y_0\big(\rho_2(\boldsymbol{x})\big) - 1/\varphi_\gamma}\right)\right], \tag{52a}$$

$$\boldsymbol{\Psi}(\boldsymbol{x}) = \begin{bmatrix}\Psi_x(\boldsymbol{x}) & \Psi_y(\boldsymbol{x})\end{bmatrix}^{\mathrm{T}} \triangleq -\tilde{\boldsymbol{u}}_{\boldsymbol{t}}\Big(\boldsymbol{x}_0\big(\rho_2(\boldsymbol{x})\big)\Big). \tag{52b}$$

The steady-state domain $\mathscr{P}^-$ may be described formally in the exact same way as done in Eq. (25), with $\Sigma(\cdot)$ reading as in Eq. (52a). In this context, it is also interesting to observe that, for the case $\big|R_\gamma\big| < a$, the steady-state solution cannot be constructed using the expression in Eq. (52a) for $\Sigma(\cdot)$, since every pair of perpendicular lines through $C_\gamma$ would lie partially inside $\mathring{\mathscr{P}}$. Moreover, even when $\big|R_\gamma\big| = a$, the function $\Sigma(\cdot)$ is not defined for $\boldsymbol{x} = \boldsymbol{x}_{C_\gamma}$.

## 4.2 Transient solution

The parametrisation $\boldsymbol{x}_0(\boldsymbol{\rho}) = \boldsymbol{\rho}$, $s_0(\boldsymbol{\rho}) = 0$ yields again the solution for the transient deflection of the bristle $\boldsymbol{u}_{\boldsymbol{t}}^+(\boldsymbol{x}, s)$:

$$\boldsymbol{u}_{\boldsymbol{t}}^+(\boldsymbol{x}, s) = \boldsymbol{\Phi}_{\varphi_\psi}(s, 0)\boldsymbol{u}_{\boldsymbol{t}0}\big(\boldsymbol{x}_0(\boldsymbol{x}, s)\big) + \int_0^s \boldsymbol{\Phi}_{\varphi_\psi}\big(s, s'\big)\Big[\boldsymbol{\sigma}\big(s'\big) + \mathbf{A}_\varphi\big(s'\big)\boldsymbol{x}\big(\boldsymbol{\rho}, s'\big)\Big]\,\mathrm{d}s', \tag{53}$$

[4]It should be noticed that the noncharacteristic conditions are always violated on the neutral edge, even for $1/\big|\varphi_\gamma\big| > a$. However, for the case under consideration, the neutral edge only consists of two single points, which have zero Lebesgue measure in $\mathscr{P}$.

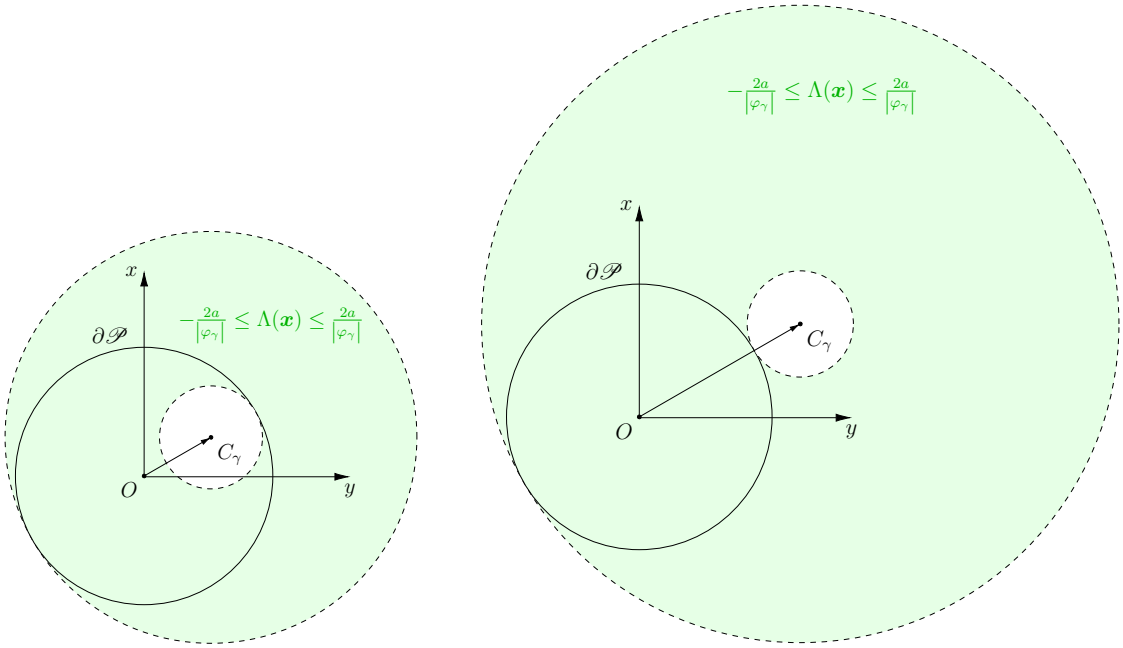


(a) Domain for the steady-state solution for $|R_\gamma| = 1/|\varphi_\gamma| < a$.

(b) Domain for the steady-state solution for $|R_\gamma| = 1/|\varphi_\gamma| > a$.

Figure 2: Valid domains for the steady-state solution $\boldsymbol{u}_{\boldsymbol{t}}^{-}(\boldsymbol{x})$ for the deflection of the bristle. The regions of the plane $\Pi$ where the requirement given by Eq. (49) is fulfilled are coloured in light green. When $|R_\gamma| = 1/|\varphi_\gamma| < a$, there exists a subregion of $\mathring{\mathscr{P}}$ where the condition (49) is violated. As a consequence, no stationary solution can be found in this region.

since the compatibility requirement imposes $\boldsymbol{\zeta}_0(\boldsymbol{\rho}(\boldsymbol{x}, s)) = \boldsymbol{u}_{\boldsymbol{t}0}(\boldsymbol{x}_0(\boldsymbol{x}, s))$. In Eq. (53), the initial coordinate vector $\boldsymbol{x}_0(\boldsymbol{x}, s)$ may be calculated by inverting Eq. (37b) as follows:

$$\boldsymbol{x}_0(\boldsymbol{x}, s) = \boldsymbol{\Phi}_{\varphi_\gamma}(0, s)\left[\boldsymbol{x} + \int_0^s \boldsymbol{\Phi}_{\varphi_\gamma}(s, s')\mathbf{A}_{\varphi_\gamma}(s')\boldsymbol{x}_{C_\gamma}(s')\,\mathrm{d}s'\right]. \tag{54}$$

For a rolling and tilting sphere, Eqs. (53) and (54) yield the most general solution for the transient deflection of the bristle under vanishing sliding conditions, whilst the case of constant slip quantities allows for additional simplification:

$$\boldsymbol{u}_{\boldsymbol{t}}^{+}(\boldsymbol{x}, s) = \mathbf{R}_{\varphi_\psi}(s)\left[\boldsymbol{u}_{\boldsymbol{t}0}\big(\boldsymbol{x}_0(\boldsymbol{x}, s)\big) - \tilde{\boldsymbol{u}}_{\boldsymbol{t}0}(\boldsymbol{x}, s)\right] + \tilde{\boldsymbol{u}}_{\boldsymbol{t}}(\boldsymbol{x}), \qquad (\boldsymbol{x}, s) \in \mathscr{P}^+ \times \mathbb{R}_{\geq 0}, \tag{55}$$

where $\tilde{\boldsymbol{u}}_{\boldsymbol{t}0}(\boldsymbol{x}, s) \triangleq \tilde{\boldsymbol{u}}_{\boldsymbol{t}}(\boldsymbol{x}_0(\boldsymbol{x}, s))$ and

$$\boldsymbol{x}_0(\boldsymbol{x}, s) = \boldsymbol{\rho}(\boldsymbol{x}, s) = \mathbf{R}_{\varphi_\gamma}^{-1}(s)\big(\boldsymbol{x} - \boldsymbol{x}_{C_\gamma}\big) + \boldsymbol{x}_{C_\gamma}. \tag{56}$$

The formal definition of the transient region of the contact patch $\mathscr{P}^+$ is analogous to that reported in Eq. (29), but clearly with $\Sigma(\cdot)$ defined as in Eq. (52a). Using the expressions for $\boldsymbol{u}_{\boldsymbol{t}}^{-}(\boldsymbol{x})$ and $\boldsymbol{u}_{\boldsymbol{t}}^{+}(\boldsymbol{x}, s)$ as given in Eqs. (51) and (55), respectively, the global solution may be patched with the same rationale as in Eq. (30), and would be $C^0(\mathscr{P} \times \mathbb{R}_{\geq 0}; \mathbb{R}^2)$ for $|R_\gamma| > a$.

# 5 Purely spinning spherical wheel

For a spinning sphere without rolling, the velocity field simplifies to $\boldsymbol{v}_{\boldsymbol{t}}(\boldsymbol{x}, t) = \mathbf{0}$. In this case, an equivalent formulation in terms of travelled distance $s$ is not possible; however, assuming that the spin speed $\dot{\psi}(t)$ does not change sign over time, dividing by $\big|\dot{\psi}(t)\big|$ and defining $\psi(t) \triangleq \int_0^t \big|\dot{\psi}(t')\big|\,\mathrm{d}t'$, the original PDEs (1) may be restated directly as a system of ODEs in the form

$$\frac{\partial \boldsymbol{u}_{\boldsymbol{t}}(\boldsymbol{x}, \psi)}{\partial \psi} = \boldsymbol{\sigma}(\psi) + \mathbf{A}_{\varphi_\psi}\big(\boldsymbol{x} + \boldsymbol{u}_{\boldsymbol{t}}(\boldsymbol{x}, \psi)\big), \qquad (\boldsymbol{x}, \psi) \in \mathring{\mathscr{P}} \times \mathbb{R}_{>0}, \tag{57}$$

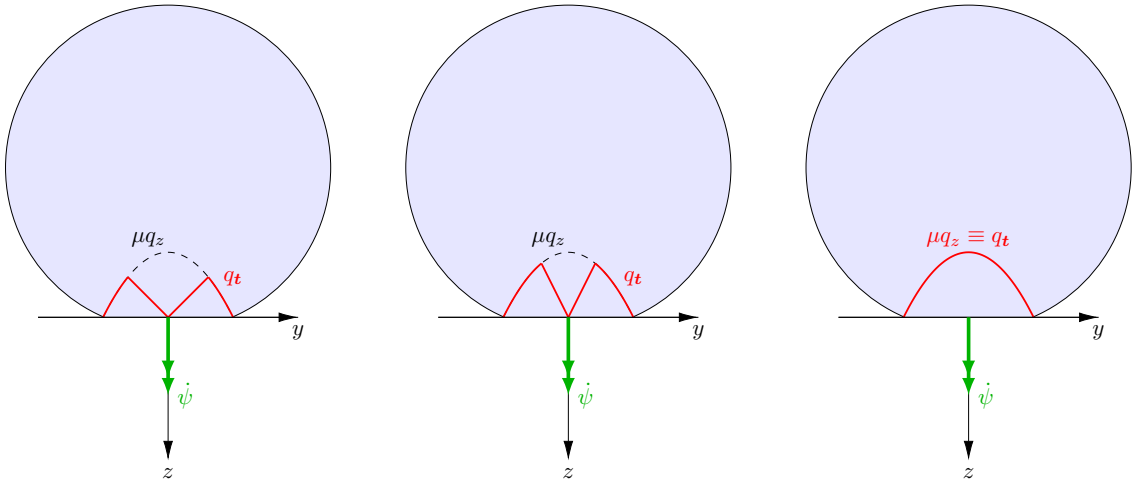


(a) $\psi = \psi^*$. (b) $\psi = 2\psi^*$. (c) $\psi \to \infty$.

Figure 3: Qualitative transient evolution of the total tangential shear stress $q_{\boldsymbol{t}}(\boldsymbol{x}, s)$ for a purely spinning spherical wheel predicted by the brush theory.

where $\boldsymbol{\sigma}(\psi) \triangleq -\boldsymbol{V}_{\mathrm{s}}(\psi)/\big|\dot\psi(\psi)\big|$ and $\varphi_\psi \triangleq -\dot\psi(\psi)/\big|\dot\psi(\psi)\big| \equiv \operatorname{sgn}(\dot\psi(\psi))$. In this context, it is worth observing that the noncharacteristic condition for the BC is violated all over $\partial\mathscr{P}$. Indeed, the neutral edge coincides with the boundary of the contact patch, that is $\mathscr{N} \equiv \partial\mathscr{P}$, and no stationary solution can be found, at least under the assumption of vanishing sliding. Thus, only the integral solution to Eq. (57) for the transient deflection of the bristle may be obtained, which reads

$$\boldsymbol{u}_{\boldsymbol{t}}(\boldsymbol{x}, \psi) \equiv \boldsymbol{u}_{\boldsymbol{t}}^{+}(\boldsymbol{x}, \psi) = \mathbf{R}_{\varphi_\psi}(\psi)\boldsymbol{u}_{\boldsymbol{t}0}(\boldsymbol{x}) + \int_0^\psi \mathbf{R}_{\varphi_\psi}(\psi')\Big[\boldsymbol{\sigma}(\psi') + \mathbf{A}_{\varphi_\psi}\boldsymbol{x}\Big]\,\mathrm{d}\psi', \tag{58}$$

where the rotation matrix $\mathbf{R}_{\varphi_\psi}(\psi)$ is given as in Eq. (40b), with the variable $s$ replaced by $\psi$, but the coordinate $\boldsymbol{x}$ is independent of the spin angle $\psi$. Moreover, similarly for the case of a rolling and tilting sphere, when the translational slip inputs are also constant, the solution reduces to

$$\boldsymbol{u}_{\boldsymbol{t}}(\boldsymbol{x}, \psi) \equiv \boldsymbol{u}_{\boldsymbol{t}}^{+}(\boldsymbol{x}, \psi) = \mathbf{R}_{\varphi_\psi}(\psi)\big[\boldsymbol{u}_{\boldsymbol{t}0}(\boldsymbol{x}) - \tilde{\boldsymbol{u}}_{\boldsymbol{t}}(\boldsymbol{x})\big] + \tilde{\boldsymbol{u}}_{\boldsymbol{t}}(\boldsymbol{x}), \qquad (\boldsymbol{x}, \psi) \in \mathscr{P} \times \mathbb{R}_{\geq 0}, \tag{59}$$

where this time $\tilde{\boldsymbol{u}}_{\boldsymbol{t}}(\boldsymbol{x}) = -\mathbf{A}_{\varphi_\psi}^{-1}\boldsymbol{\sigma} - \boldsymbol{x}$.

The solutions derived in Eqs. (60) and (59) are still acceptable owing to the assumption of vanishing sliding. However, it is worth mentioning that, if the contribution relating to the deflection of the bristle is neglected in the right-hand side of Eq. (57), the integral (60) becomes

$$\boldsymbol{u}_{\boldsymbol{t}}(\boldsymbol{x}, \psi) \equiv \boldsymbol{u}_{\boldsymbol{t}}^{+}(\boldsymbol{x}, \psi) = \boldsymbol{u}_{\boldsymbol{t}0}(\boldsymbol{x}) + \int_0^\psi \boldsymbol{\sigma}(\psi')\,\mathrm{d}s' + \mathbf{A}_{\varphi_\psi}\boldsymbol{x}\psi, \tag{60}$$

which may grow unbounded with $\psi$ even when the slip inputs are constant. To exemplify this aspect, it is sufficient to consider a situation with zero slip inputs, i.e. $\boldsymbol{\sigma} = \mathbf{0}$. The initial configuration might also be assumed to be undeformed for simplicity, that is $\boldsymbol{u}_{\boldsymbol{t}0}(\boldsymbol{x}) = \mathbf{0}$. According to Eq. (60), the total transient stress acting at coordinate $\boldsymbol{x}$ becomes $q_{\boldsymbol{t}}^{+}(\boldsymbol{x}, \psi) = k\big|\varphi_\psi\big|\|\boldsymbol{x}\|\,\psi$, which increases linearly with the spin angle $\psi$. The issues introduced by the simplified formulation might be overcome by assuming limited friction inside the contact patch. In this case, a constant traction bound $\mu q_z(\boldsymbol{x})$ would impose a limit on the value assumed by the total stress $q_{\boldsymbol{t}}^{+}(\boldsymbol{x}, \psi)$, and a steady-state solution could be recovered from the corresponding limiting distribution. The situation is illustrated schematically in Fig. 3, where the evolution of the shear stresses acting inside the contact patch is plotted for three different values of $\psi$, starting from an initial undeformed configuration.

In this context, it should be noticed that, owing to the condition $\partial\boldsymbol{u}_{\boldsymbol{t}}^{(\mathrm{s})}(\boldsymbol{x})/\partial\psi = \mathbf{0}$ in the sliding zone, the direction of the tangential shear stress in $\mathscr{P}^{(\mathrm{s})}$ may be deduced directly from the right-hand side of Eq. (57) (when the contribution of $\boldsymbol{u}_{\boldsymbol{t}}(\boldsymbol{x}, \psi)$ is neglected). Moreover, since $\boldsymbol{q}_{\boldsymbol{t}}^{(\mathrm{s})}(\boldsymbol{x})$ is opposed

to the sliding velocity according to Eq. (4b), and the latter vanishes for $\boldsymbol{x} = \boldsymbol{x}_{C_{\varphi_\psi}} = -\mathbf{A}_{\varphi_\psi}^{-1}\boldsymbol{\sigma}$, where $C_{\varphi_\psi}$ denotes the spin centre, it follows that that the sliding solution is not defined for $\boldsymbol{x} = \boldsymbol{x}_{C_{\varphi_\psi}}$. For $\boldsymbol{\sigma} = \mathbf{0}$, the position of the spin centre coincides with the origin of the contact patch, i.e. $C_{\varphi_\psi} \equiv O$, as it happens in Fig. 3. Therefore, the fact that the transient shear stress $\boldsymbol{q}_{\boldsymbol{t}}^{+}(\boldsymbol{x}, \psi)$ never reaches the traction bound at the origin should not be surprising, since this condition only preserves the well-posedness of the problem for any finite value of $\psi$. Similar considerations also hold when $\boldsymbol{\sigma} \neq \mathbf{0}$, provided to start from an undeformed initial configuration $\boldsymbol{u}_{\boldsymbol{t}0}(\boldsymbol{x}) = \mathbf{0}$.

# 6 Steady-state characteristics

The steady-state tangential forces $\boldsymbol{F}_{\boldsymbol{t}} = F_x\hat{\boldsymbol{e}}_x + F_y\hat{\boldsymbol{e}}_y$ and moment $M_z$ generated by the rolling of the spherical wheel may be computed by direct integration over the contact patch $\mathscr{P}$ starting from the known expression for the stationary deflection of the bristle $\boldsymbol{u}_{\boldsymbol{t}}^{-}(\boldsymbol{x})$ derived in Sects. 3 and 4. Specifically, under the assumption of vanishing sliding, the following expressions may be deduced for the case of a purely rolling sphere with $\varepsilon_x = 0$, $\varepsilon_y = 1$:

$$\boldsymbol{F}_{\boldsymbol{t}}(\boldsymbol{\sigma}, \varphi) = C_\sigma\boldsymbol{\sigma} + C_\varphi\varphi\hat{\boldsymbol{e}}_y, \tag{61a}$$

$$M_z(\sigma_y) = -C_{M\sigma_y}\sigma_y, \tag{61b}$$

with

$$C_\sigma = \frac{8}{3}ka^3 \qquad \text{and} \qquad C_\varphi = C_{M\sigma_y} = \frac{3\pi a}{32}C_\sigma. \tag{62}$$

It should be observed that, owing to the assumptions of circular contact patch and isotropic material, in steady-state conditions, the original reference frame may always be re-oriented to yield $\varepsilon_x = 0$, $\varepsilon_y = 1$ (which implies that the $x$ axis points towards the direction of motion). However, in the more stringent case of limited friction, closed-form representations for the forces and moment are almost impossible to derive when accounting for the presence of combined translational and spin slips, and the shear stresses need to be integrated numerically. The same procedure must be employed also for the case of rolling and tilting spherical wheel analysed in Sect. 4. To this end, an expression for the steady-state vertical pressure distribution $q_z(\boldsymbol{x})$ need to be specified, and the direction of the shear stresses in the sliding zone may initially be approximated neglecting the contribution of $\boldsymbol{u}_{\boldsymbol{t}}(\boldsymbol{x})$ in the calculation of the sliding velocity [18].

In Fig. 4(a) and (b), the trends of the tangential forces $\boldsymbol{F}_{\boldsymbol{t}}$ and moment $M_z$ are plotted versus the longitudinal slip variable $\sigma_x$ for different combinations of lateral slips $\sigma_y$ (again for $\varepsilon_x = 0$, $\varepsilon_y = 1$). The value for the total tilt spin is $\varphi = 3.33$ m$^{-1}$, with $\chi_\gamma = 0.9$. The vertical pressure distribution $q_z(\boldsymbol{x})$ acting inside the contact is assumed to be parabolic, corresponding to a total vertical load of $F_z = 3000$ N and contact patch radius of $a = 0.05$ m. Finally, the bristle stiffness is $k = 1.023 \cdot 10^8$ N m$^{-3}$. In particular, the solid lines refer to the steady-state characteristics calculated according to the expression $\boldsymbol{u}_{\boldsymbol{t}}^{-}(\boldsymbol{x})$ derived in Sect. 3, whereas the dashed ones to those computed using the solution deduced in Sect. 4. No substantial difference may be observed between the two formulations, mostly due to the high values of the tilting radius $R_\gamma$, and the approximation commited in the calculation of the sliding direction.

Figure 4(c) illustrates the trend of the lateral force $F_y$ versus the longitudinal one $F_x$. In Vehicle Dynamics, this type of plot is often referred to as *the friction circle*. The physical interpretation of Fig. 4(c) is that the maximum available friction $\mu F_z$ inside the contact patch may be distributed between the longitudinal and lateral characteristics. These two represent the projections of the maximum attainable force $\mu F_z$ along the $x$ and $y$ directions, respectively. For anisotropic bodies, the friction circle becomes more generally an ellipse.

# 7 Discussion and conclusions

This paper investigated the dynamics of a spherical wheel within the theoretical framework provided by the brush models. As opposed to most works in which a unique contact point is assumed between the rolling sphere and the supporting plane, the present analysis considered the more general situation of a finite contact area. Accordingly, the investigation was divided into three main parts, depending on the structure of the tangential velocity field inside the contact patch.

The first part of the study in Sect. 3 was hence devoted to the problem of a rolling spherical wheel with no tilting. In particular, the general solution to the governing PDEs of the brush models was provided in

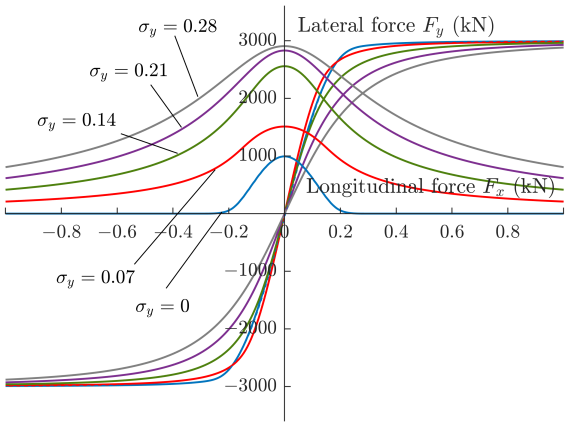


(a) Longitudinal and lateral forces $F_x$, $F_y$ versus longitudinal slip $\sigma_x$.

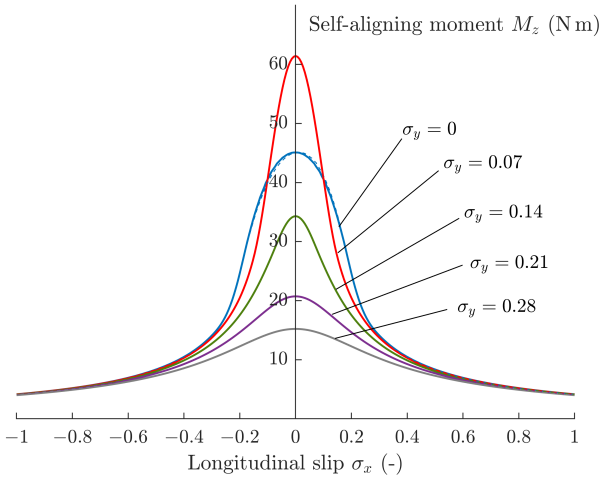


(b) Self-aligning moment $M_z$ versus longitudinal slip $\sigma_x$.

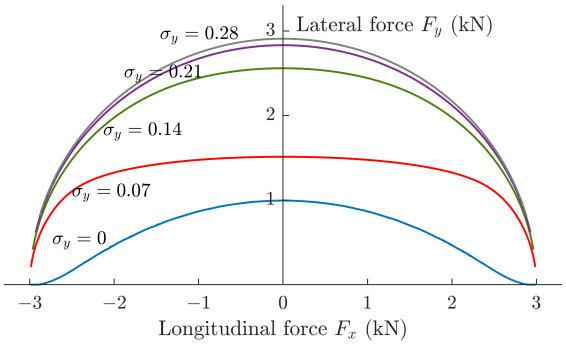


(c) Lateral force $F_y$ versus longitudinal force $F_x$.

Figure 4: Steady-state characteristics predicted for the rolling spherical wheel of Sect. 3 (solid lines) and the rolling and tilting spherical wheel of Sect. 4 (dashed lines) for different values of the lateral slip $\sigma_y$. Note that, given the striking match between the steady-state characteristics predicted by the two approaches, the dashed lines overlap almost completely with the solid ones. Parameters: $\varphi = 3.33$ m$^{-1}$, $\chi_\gamma = 0.9$, $F_z = 3000$ N, $a = 0.05$ m, $\mu = 1$.

terms of a linear system of ODEs. Closed-form representations for the deflection of the bristles were then derived in respect to the steady-state and transient cases separately. In this context, it was also shown that the deformation is continuous at the transition between the steady-state and transient regions of the contact patch, which implies the existence of weak solutions to the system of PDEs governing the brush models. This aspect is relatively important, considering that it is often impossible to recover classic solutions even in case of vanishing sliding conditions. Analogous conclusions about the well-posedness of the brush models were drawn from a straightforward application of the energy method, presented in Appendix B.

In Sect. 4, the analysis was then extended to the situation of a rolling and tilting sphere. A similar procedure was applied to recover both the stationary and time-varying solutions. For a rolling sphere with tilting and contact patch radii given by $\left|R_\gamma\right|$ and $a$, respectively, a major difference with the case of a simply rolling sphere was that steady-state solutions could not be determined inside the whole contact patch unless the condition $\left|R_\gamma\right| \geq a$ was satisfied. This phenomenon may be explained within the theoretical framework of the brush models by observing that, when the condition $\left|R_\gamma\right| < a$ holds, there exists an inner circle inside $\mathscr{P}$ for which the bristles are not able to enter nor relinquish the contact patch itself. Therefore, these bristles travel describing a circular trajectory around the tilting centre $C_\gamma$, and never reach steady-state conditions.

Then, in Sect. 5, the problem of a pure spinning spherical wheel was investigated. It was found that, owing to the assumption of vanishing sliding, steady-state conditions are always impossible to obtain. Moreover, it was shown that neglecting second-order terms in the computation of the sliding velocity leads to unbounded solutions for the deflection of the bristle. This aspect was further clarified using a simple example. For the case of a pure spinning spherical wheel, it appears that the Amontons-Coulomb friction model generally preserves the well-posedness of the problem, but different formulations may also be explored to cope with more complex scenarios.

The qualitative trend for the steady-state characteristics predicted using the solutions derived in Sects. 3 and 4 was finally provided in Sect. 6. No substantial discrepancies could be observed between the results yielded by the two different formulations, mainly due to the fact that an approximated expression for the sliding direction was employed when determining the bristle deflection in the sliding zone.

The results advocated in the paper may be used as a starting point to develop slip-based equations to describe the forces generated inside the contact patch, similar to those employed in tyre dynamics [18]. Such a description would be particularly useful for control applications involving spherical robots and wheels. Additional research efforts must therefore be directed towards model validation by comparison with more accurate formulations, and to the development of *ad-hoc* formulae.

## Compliance with Ethical Standards

The authors declare that they have no conflict of interest.

## Acknowledgments

The authors gratefully acknowledge financial support from the COVER project (44929-1), funded by the Swedish energy agency and the Swedish vehicle research and innovation program (FFI).

## Nomenclature

| **Forces and Moments** | **Unit** | **Description** |
|---|---|---|
| $\boldsymbol{q_t}$ | $\mathrm{N\,m^{-2}}$ | Tangential shear stress vector |
| $q_{\boldsymbol{t}}$ | $\mathrm{N\,m^{-2}}$ | Total tangential shear stress |
| $q_x$, $q_y$ | $\mathrm{N\,m^{-2}}$ | Longitudinal and lateral shear stress |
| $\boldsymbol{q_t^-}$ | $\mathrm{N\,m^{-2}}$ | Steady-state shear stress vector |
| $q_x^-$, $q_y^-$ | $\mathrm{N\,m^{-2}}$ | Steady-state longitudinal and lateral shear stresses |
| $\boldsymbol{q_t^+}$ | $\mathrm{N\,m^{-2}}$ | Transient shear stress vector |
| $q_x^+$, $q_y^+$ | $\mathrm{N\,m^{-2}}$ | Transient longitudinal and lateral shear stresses |

| **Displacements** | **Unit** | **Description** |
|---|---|---|
| $\boldsymbol{u_t}$ | m | Displacement vector of the bristle |
| $u_x$, $u_y$ | m | Longitudinal and lateral displacement of the bristle |
| $\boldsymbol{u_t^-}$ | m | Steady-state tangential displacement vector of the bristle |
| $u_x^-$, $u_y^-$ | m | Steady-state longitudinal and lateral displacement |
| $\boldsymbol{u_t^+}$ | m | Transient tangential displacement vector of the bristle |
| $u_x^+$, $u_y^+$ | m | Transient longitudinal and lateral displacement |
| $\boldsymbol{u_{t0}}$ | m | Initial tangential displacement vector of the bristle (IC) |
| $u_{x0}$, $u_{y0}$ | m | Initial longitudinal and lateral displacement (IC) |
| $s$ | m | Travelled distance |
| $t$ | s | Time |
| $\psi$ | rad | Turn angle |
| $\boldsymbol{x}$ | m | Coordinate vector |
| $x$, $y$, $z$ | m | Longitudinal, lateral and vertical coordinates |
| $\boldsymbol{x}_0$ | m | Initial data coordinate vector |
| $x_0$, $y_0$ | m | Initial longitudinal and lateral coordinates |

| **Speeds** | **Unit** | **Description** |
|---|---|---|
| $\boldsymbol{v_t}$ | $\mathrm{m\,s^{-1}}$ | Tangential velocity field |
| $v_x$, $v_y$ | $\mathrm{m\,s^{-1}}$ | Longitudinal and lateral components of the tangential velocity field |
| $\bar{\boldsymbol{v}}_{\boldsymbol{t}}$ | - | Nondimensional tangential velocity field |
| $\bar{v}_x$, $\bar{v}_y$ | - | Longitudinal and lateral components of the nondimensional velocity field |
| $\boldsymbol{v}_{\mathrm{s}}$ | $\mathrm{m\,s^{-1}}$ | Micro-sliding velocity |
| $v_{\mathrm{s}x}$, $v_{\mathrm{s}y}$ | $\mathrm{m\,s^{-1}}$ | Longitudinal and lateral micro-sliding speeds |
| $\boldsymbol{V}_C$ | $\mathrm{m\,s^{-1}}$ | Contact patch centre velocity |
| $V_{Cx}$, $V_{Cy}$ | $\mathrm{m\,s^{-1}}$ | Longitudinal and lateral speeds of the contact patch centre |
| $\boldsymbol{V}_O$ | $\mathrm{m\,s^{-1}}$ | Velocity of the origin $O$ |
| $\boldsymbol{V}_{\mathrm{r}}$ | $\mathrm{m\,s^{-1}}$ | Rolling velocity |
| $V_{\mathrm{r}}$ | $\mathrm{m\,s^{-1}}$ | Rolling speed |
| $\boldsymbol{V}_{\mathrm{s}}$ | $\mathrm{m\,s^{-1}}$ | Sliding velocity |
| $V_{\mathrm{s}x}$, $V_{\mathrm{s}y}$ | $\mathrm{m\,s^{-1}}$ | Longitudinal and lateral sliding speeds |
| $\dot{\psi}$ | $\mathrm{rad\,s^{-1}}$ | Turning speed |
| $\boldsymbol{\omega}$ | $\mathrm{rad\,s^{-1}}$ | Angular speed vector |
| $\omega_x$, $\omega_y$, $\omega_\gamma$ | $\mathrm{rad\,s^{-1}}$ | Longitudinal, lateral and tilting angular speeds |
| $\omega_z$ | $\mathrm{rad\,s^{-1}}$ | Total vertical angular speed |

| **Slip Parameters** | **Unit** | **Description** |
|---|---|---|
| $\boldsymbol{\varepsilon}$ | - | Constant vector component of the nondimensional velocity field |
| $\varepsilon_x$, $\varepsilon_y$ | - | Longitudinal and lateral constant components of the nondimensional velocity field |
| $\chi_\gamma$, $\chi_\psi$ | - | Tilt and turn ratio |
| $\boldsymbol{\sigma}$ | - | Translational slip vector |
| $\sigma_x$, $\sigma_y$ | - | Longitudinal and lateral slip |
| $\varphi$ | $\mathrm{m^{-1}}$ | Rotational slip or spin parameter |
| $\varphi_\gamma$, $\varphi_\psi$ | $\mathrm{m^{-1}}$ | Tilt and turn spin parameters |

| **Matrices and Tensors** | **Unit** | **Description** |
|---|---|---|
| $\mathbf{A}_{\omega_z}$, $\mathbf{A}_{\omega_\gamma}$ | $\mathrm{rad\,s^{-1}}$ | Total vertical angular speed and tilt speed tensors |
| $\mathbf{A}_\varphi$, $\mathbf{A}_{\varphi_\gamma}$, $\mathbf{A}_{\varphi_\psi}$ | $\mathrm{m^{-1}}$ | Spin, tilt spin and turn spin tensors |
| $\mathbf{R}_{\varphi_\gamma}$ | - | Tilt spin rotation matrix |
| $\mathbf{R}_{\varphi_\psi}$ | - | Turn spin rotation matrix |
| $\boldsymbol{\Phi}_{\varphi_\gamma}$ | - | Transition matrix for tilt spin |
| $\boldsymbol{\Phi}_{\varphi_\psi}$ | - | Transition matrix for turn spin |

| **Geometric** | **Unit** | **Description** |
|---|---|---|

| **Parameters** | | |
|---|---|---|
| $a$, $b$ | m | Contact patch semilength and semiwidth |
| $\boldsymbol{x}_{C_\gamma}$, $\boldsymbol{x}_{C_\psi}$ | m | Tilting centre and turning centre coordinate vectors |
| $x_{C_\gamma}$, $x_{C_\psi}$ | m | Tilting centre and turning centre longitudinal coordinates |
| $y_{C_\gamma}$, $y_{C_\psi}$ | m | Tilting centre and turning centre lateral coordinates |
| $x_{\mathscr{L}}$, $y_{\mathscr{L}}$ | m | Leading edge explicit representations |
| $R_\mathrm{r}$ | m | Rolling radius |
| $R_\gamma$, $R_\psi$ | m | Tilting radius and turning radius |

| **Stiffnesses and Compliances** | **Unit** | **Description** |
|---|---|---|
| $k$ | $\mathrm{N\,m^{-3}}$ | Bristle stiffness |

| **Functions and Operators** | **Unit** | **Description** |
|---|---|---|
| $\nabla_{\boldsymbol{t}}$ | $\mathrm{m^{-1}}$ | Tangential gradient |
| $\Gamma(\cdot)$ | $\mathrm{m^2}$ | Gamma function |
| $\Sigma(\cdot)$ | m | Sigma function |
| $\boldsymbol{\Psi}(\cdot)$ | m | Vector-valued psi function |
| $\Psi_x(\cdot)$, $\Psi_y(\cdot)$ | m | Longitudinal and lateral psi functions |

| **Sets** | **Unit** | **Description** |
|---|---|---|
| $\mathscr{P}$ | $\mathrm{m^2}$ | Contact patch |
| $\mathscr{P}_0$ | $\mathrm{m^2}$ | Initial condition for the contact patch |
| $\mathscr{P}^-$ | $\mathrm{m^2}$ | Steady-state zone |
| $\mathscr{P}^+$ | $\mathrm{m^2}$ | Transient zone |
| $\mathring{\mathscr{P}}$ | $\mathrm{m^2}$ | Interior of $\mathscr{P}$ |
| $\mathring{\mathscr{P}}_0$ | $\mathrm{m^2}$ | Initial condition for $\mathring{\mathscr{P}}$ |
| $\partial\mathscr{P}$ | m | Boundary of $\mathscr{P}$ |
| $\partial\mathscr{P}_0$ | m | Initial condition for the boundary $\partial\mathscr{P}$ |
| $\mathscr{L}$ | m | Leading edge |
| $\mathscr{L}_0$ | m | Initial condition for the leading edge |
| $\mathscr{N}$ | m | Neutral edge |
| $\mathscr{S}$ | m | Sliding edge |
| $\mathscr{T}$ | m | Trailing edge |
| $\mathbb{R}_{\geq 0}$ | - | Set of positive real numbers (including 0) |
| $\mathbb{R}_{>0}$ | - | Set of strictly positive real numbers (excluding 0) |

| **Implicit curves** | **Unit** | **Description** |
|---|---|---|
| $\gamma_\Sigma$ | m | Implicit representation of the travelling edge |

# References


[1] Zheng M, Zhan Q, Liu J, Cai Y. Control of a Spherical Robot: Path Following Based on Nonholonomic Kinematics and Dynamics. Chinese Journal of Aeronautics. 2011;23(3):337-345. Available from: https://doi.org/10.1016/S1000-9361(11)60040-X.

[2] Karavaev YL, Kilin AA. The dynamics and control of a spherical robot with an internal omni-wheel platform. Regul. Chaot. Dyn. 2015;20:134–152. Available from: https://doi.org/10.1134/S1560354715020033.

[3] Ba PD, Dong Hoang Q, Lee SG, Nguyen TH, Quang Duong X, Tham BC. Kinematic Modeling of Spherical Rolling Robots with a Three-Omnidirectional-Wheel Drive Mechanism. 2020 20th International Conference on Control, Automation and Systems (ICCAS) 2020. pp. 463-466. Available from: https//doi:10.23919/ICCAS50221.2020.9268200.

[4] Ghariblu H, Mohammadi H. Structure and dynamic modelling of a spherical robot. 2012 8th International Symposium on Mechatronics and its Applications. 2012. pp. 1-5. Available from: https//doi:10.1109/ISMA.2012.6215159.

[5] Hogan FR, Forbes JR. Modeling of spherical robots rolling on generic surfaces. Multibody Syst Dyn. 2015;35:91–109. Available from: https://doi.org/10.1007/s11044-014-9438-3.

[6] Zhuang W, Liu X, Fang C, Sun H. Dynamic Modeling of a Spherical Robot with Arms by Using Kane's Method. 2008 Fourth International Conference on Natural Computation. 2008. pp. 373-377. Available from: https//doi:10.1109/ICNC.2008.595.
[7] Moazami S, Zargarzadeh H, Palanki S. Kinematics of Spherical Robots Rolling over 3D Terrains. Complexity. 2019. Article ID 7543969, 14 pages. Available from: https://doi.org/10.1155/2019/7543969.
[8] Knothe K, Groß-Thebing A. Short wavelength rail corrugation and non-steady-state contact mechanics. Vehicle Syst. Dyn. 2008;46(1-2):49-66. Available from: https://doi.org/10.1080/00423110701590180.
[9] Alonso A, Giménez JG. Non-steady state modelling of wheel-rail contact problem for the dynamic simulation of railway vehicles. Vehicle Syst. Dyn. 2008;46(3):179-196. Available from: https://doi.org/10.1080/00423110701248011.
[10] Guiral A, Alonso A, Baeza L,Giménez JG. Non-steady state modelling of wheel–rail contact problem, Vehicle System Dynamics. 2013;51(1):91-108. Available from: https://doi.org/10.1080/00423114.2012.713499.
[11] Cattaneo C. Sul contatto di due corpi elastici: distribuzione locale degli sforzi. Rendiconti dell'Accademia Naturale dei Lincei. 2008; Serie 6, 227, 342-348, 434-436, 474-478.
[12] Zhuravlev, V.P., Klimov, D.M.: Global motion of the celt. Mech. Solids 43(3), 320–327 (2008).
[13] Kudra G, Awrejcewicz J, 2019. Rolling resistance modelling in the Celtic stone dynamics. Multibody Syst Dyn; 45:155-167. Available from: https://doi.org/10.1007/s11044-018-9624-9.
[14] Kalker JJ. Three-Dimensional Elastic Bodies in Rolling Contact. Springer: Dordrecht; 1990. https://doi.org/10.1007/978-94-015-7889-9.
[15] Kalker JJ. Rolling Contact Phenomena. In: Jacobson B., Kalker J. J. (eds) Rolling Contact Phenomena. International Centre for Mechanical Sciences (Courses and Lectures), vol 411. Springer, Vienna
[16] Zaazaa KE, Schwab AL. Review of Joost Kalker's wheel-rail contact theories and their implementation in multibody codes. Proceedings of the ASME 2009 International Design Engineering Technical Conferences & Computers and Information In Engineering Conference IDETC/CIE 2009; San Diego, California, USA; 2009.
[17] Meymand SZ, Keylin A, Ahmadian M. A survey of wheel-rail contact models for rail vehicles. Vehicle Syst. Dyn. 2016;54(3):386-428.
[18] Pacejka HB. Tire and vehicle dynamics. 3rd ed. Amsterdam: Elsevier/BH; 2012.
[19] Kalker JJ. railway wheel and automotive tyre. Vehicle Syst. Dyn. 1979;5(15):255-269.
[20] Contensou P. Couplage entre frottement de glissement et de pivotement dans la téorie de la toupe. In: Ziegler, H. (ed.) Kreiselprobleme Gyrodynamic, IUTAM Symposium Celerina, pp. 201–216. Springer, Berlin (1962).
[21] Zhuravlev, V.P., 1998. The model of dry friction in the problem of the rolling of rigid bodies. Journal of Applied Mathematics and Mechanics 62 (5), 705e710.
[22] Zhuravlev, V.P., 2003. Friction laws in the case of combination of slip and spin. Mechanics of Solids 38 (4), 52e58.
[23] Kireenkov, A.A., 2005. About the motion of the symmetric rigid solid along the plane. In: 8th Conference on DSTA, pp. 95e102.
[24] Kireenkov, A.A., 2008. Combined model of sliding and rolling friction in dynamics of bodies on a rough plane. Mechanics of Solids 43 (3), 412e425.
[25] Leine RI, Glocker C, 2003. A set-valued force law for spatial Coulomb-Contensou friction. European Journal of Mechanics A/Solids 22 (2), 193e216.
[26] Kudra G, Awrejcewicz J, 2013. Approximate modelling of resulting dry friction forces and rolling resistance for elliptic contact shape. European Journal of Mechanics A/Solids 42, pp. 358-75.
[27] Fromm H. Berechnung des Schlupfes beim Rollen deformierbarer Scheiben.
[28] Kalker JJ, Dekking FM, Vollebregt EAH. Simulation of rough, elastic contact. Journal of Applied Mechanics. 1997; 64/361.
[29] Kalker JJ. On the rolling contact of two elastic bodies in the presence of dry friction [doctoral thesis]. Delft; 1967.
[30] Kalker JJ. Transient rolling contact phenomena. ASLE Trans. 1971;14(3):177-184. Available from: https://doi.org/10.1080/05698197108983240.
[31] Kalker JJ. Transient phenomena in two elastically similar rolling cylinders in the presence of dry friction," University of Technology, Delft, WTHD Rept. 11, (1969)
[32] Guiggiani M. The Science of Vehicle Dynamics, 2nd ed. Cham(Switzerland): Springer International;

2018.
[33] Limebeer DJN, Massaro M. Dynamics and Optimal Control of Road Vehicle. Oxford University Press; 2018.
[34] Sakai H. Study on cornering properties of tire and vehicle. Tire Science and Technology 1990;18(3):136–169. Available from: https://doi.org/10.2346/1.2141697.
[35] Romano L, Sakhnevych A, Strano S et al. A novel brush-model with flexible carcass for transient interactions. Meccanica. 2019;54:1663–1679. Available from: https://doi.org/10.1007/s11012-019-01040-0.
[36] Kalker JJ. Survey of wheel-rail rolling contact theory. Vehicle Syst Dyn. 1997;8(4):317-358. Available from: https://doi.org/10.1080/00423117908968610 .
[37] Romano L, Bruzelius F Jacobson B. Unsteady-state brush theory. Vehicle Syst. Dyn. 2020; pages 1-29. Available from: https://doi.org/10.1080/00423114.2020.1774625.
[38] Romano L, Bruzelius F Jacobson B. Brush tyre models for large camber angles and steering speeds. Vehicle Syst Dyn. 2020; pages 1-52. Available from: https://doi.org/10.1080/00423114.2020.1854320.
[39] Romano L, Timpone F, Bruzelius F, Jacobson B. Analytical results in transient brush tyre models: theory for large camber angles and classic solutions with limited friction. Meccanica. Available from: https://doi.org/10.1007/s11012-021-01422-3.
[40] Frendo F, Bucchi F. "Brush model" for the analysis of flat belt transmissions in steady-state conditions. Mechanism and Machine Theory. 2020. 143. Available from https://doi.org/10.1016/j.mechmachtheory.2019.103653.
[41] Frendo F, Bucchi F. Enhanced brush model for the mechanics of power transmission in flat belt drives under steady–state conditions: Effect of belt elasticity. Mechanism and Machine Theory. 2020. 153. Available from: https://doi.org/10.1016/j.mechmachtheory.2020.103998.
[42] Bucchi F, Frendo F. Validation of the brush model for the analysis of flat belt transmissions in steady-state conditions by finite element simulation. Mechanism and Machine Theory. 2022. 167. Available from: https://doi.org/10.1016/j.mechmachtheory.2021.104556.
[43] Persson BNJ. Theory of rubber friction and contact mechanics. The Journal of Chemical Physics 2001;115(8):3840-3861. Available from: https://doi.org/10.1063/1.1388626.
[44] Persson BNJ, Albohr O, Tartaglino U, Volokitin AI, Tosatti E. On the nature of surface roughness with application to contact mechanics, sealing, rubber friction and adhesion. Journal of Physics: Condensed Matter 20004;17(1):R1-R62.
[45] Persson BNJ. Contact mechanics for randomly rough surfaces. Surface Science Reports. 2006;61(4):201-227. Available from: https://doi.org/10.1016/j.surfrep.2006.04.001.
[46] O'Neill A, Gruber P, Watts JF, Prins J. Predicting Tyre Behaviour on Different Road Surfaces. In: Klomp M, Bruzelius F, Nielsen J, Hillemyr A. (eds) Advances in Dynamics of Vehicles on Roads and Tracks. IAVSD 2019. Lecture Notes in Mechanical Engineering. Springer, Cham. Available from: https://doi.org/10.1007/978-3-030-38077-9_215.
[47] O'Neill A, Prins J, Watts JF, Gruber P. Enhancing brush tyre model accuracy through friction measurements. Vehicle Syst. Dyn. 2021; pag. 1-23. Available from: https://doi.org/10.1080/00423114.2021.1893766.
[48] Heinrich G, Klüppel M. Rubber friction, tread deformation and tire traction. Wear. 2008;265(7-8):1052-1060. Available from: https://www.sciencedirect.com/science/article/pii/S0043164808000847.
[49] Duvaut G, Lions JL. Inequalities in Mechanics and Physics. Springer-Verlag: Berlin Heidelberg; 1976. Available from: https://doi.org/10.1007/978-3-642-66165-5.
[50] Kalker JJ. Variational Principles of Contact Elastostatics. J. Inst. Maths. Applics. 1997;20:199-219.
[51] Evans LC. Partial differential equations. 2nd ed. American Mathematical Society; 1996.
[52] Ockendon JR, Howison S, Lacey A, Movchan A. Applied partial differential equations. Oxford University Press; 2003.
[53] Polyanin AD, Manzhirov AV. Handbook of mathematics for engineers and scientists. Boca Raton–London: Chapman & Hall/CRC Press; 2007.
[54] Pacejka HB. Spin: camber and turning. Vehicle Syst Dyn. 2005;43(1):3-17. Available from https://doi.org/10.1080/00423110500140013.
[55] Rugh, WJ. Linear System Theory. 2nd ed. Johns Hopkins University; 2007.
[56] Khalil HK. Nonlinear Systems. 3rd ed. Prentice Hall, Upper Saddle River; 2002.
[57] Truesdell C, Toupin RA. The classical field theories. In Flügge S, editor, Handbuch der Physik, vol. 3/1, page 226. Springer-Verag: Berlin; 1960.

[58] Truesdell C, Rajagopal KR. An Introduction to the Mechanics of Fluids. Birkhäuser Boston 2000. Available from: https://doi.org/10.1007/978-0-8176-4846-6.

# A Velocity of the boundary of the contact patch

An expression for the velocity of the boundary of the contact patch may be derived by resorting to some some basic results from differential geometry. First, it may be observed that the product $\boldsymbol{v}_{\partial\mathscr{P}}(\boldsymbol{x},t)\cdot\hat{\boldsymbol{\nu}}_{\partial\mathscr{P}}(\boldsymbol{x},t)$ represents a velocity of the boundary of the contact patch that is oriented as the unit normal. Thus, describing the boundary $\partial\mathscr{P}$ in implicit form as

$$\partial\mathscr{P}=\big\{\boldsymbol{x}\in\mathit{\Pi}\;\big|\;\gamma_{\partial\mathscr{P}}(\boldsymbol{x},t)=0\big\},\tag{63}$$

the expression for the outward-pointing unit normal to $\partial\mathscr{P}$ may be deduced as follows:

$$\hat{\boldsymbol{\nu}}_{\partial\mathscr{P}}(\boldsymbol{x},t)=\pm\frac{\nabla_{\boldsymbol{t}}\gamma_{\partial\mathscr{P}}(\boldsymbol{x},t)}{\big\|\nabla_{\boldsymbol{t}}\gamma_{\partial\mathscr{P}}(\boldsymbol{x},t)\big\|}.\tag{64}$$

Furthermore, differentiating $\gamma_{\partial\mathscr{P}}(\boldsymbol{x},t)$ with respect to the time variable following a point on the contact patch boundary yields [57, 58]

$$\frac{\partial\gamma_{\partial\mathscr{P}}(\boldsymbol{x},t)}{\partial t}+\boldsymbol{v}^{(\boldsymbol{\rho})}_{\partial\mathscr{P}}(\boldsymbol{\rho},t)\cdot\nabla_{\boldsymbol{t}}\gamma_{\partial\mathscr{P}}(\boldsymbol{x},t)=0,\tag{65}$$

where the velocity $\boldsymbol{v}^{(\boldsymbol{\rho})}_{\partial\mathscr{P}}(\boldsymbol{\rho},t)$ may be computed starting from a parametric representation of the contact patch boundary. It follows that

$$\boldsymbol{v}^{(\boldsymbol{\rho})}_{\partial\mathscr{P}}(\boldsymbol{\rho},t)\cdot\hat{\boldsymbol{\nu}}_{\partial\mathscr{P}}(\boldsymbol{x},t)=\boldsymbol{v}_{\partial\mathscr{P}}(\boldsymbol{x},t)\cdot\hat{\boldsymbol{\nu}}_{\partial\mathscr{P}}(\boldsymbol{x},t)=\mp\frac{1}{\big\|\nabla_{\boldsymbol{t}}\gamma_{\partial\mathscr{P}}(\boldsymbol{x},t)\big\|}\,\frac{\partial\gamma_{\partial\mathscr{P}}(\boldsymbol{x},t)}{\partial t}\,.\tag{66}$$

A particular representation of the velocity of the contact patch boundary that is oriented as the unit normal may be thus derived as

$$\boldsymbol{v}^{(\hat{\boldsymbol{\nu}})}_{\partial\mathscr{P}}(\boldsymbol{x},t)\triangleq-\frac{\nabla_{\boldsymbol{t}}\gamma_{\partial\mathscr{P}}(\boldsymbol{x},t)}{\big\|\nabla_{\boldsymbol{t}}\gamma_{\partial\mathscr{P}}(\boldsymbol{x},t)\big\|^2}\,\frac{\partial\gamma_{\partial\mathscr{P}}(\boldsymbol{x},t)}{\partial t}\,.\tag{67}$$

**Example A.1.** *For the circular contact patch assumed in the paper, the boundary $\partial\mathscr{P}$ admits an implicit representation of the form as in Eq. (63), with $\gamma_{\partial\mathscr{P}}(\boldsymbol{x},t)=x^2+y^2-a^2(t)=0$. Accordingly, straightforward calculations yield the following expression for the velocity $\boldsymbol{v}^{(\hat{\boldsymbol{\nu}})}_{\partial\mathscr{P}}(\boldsymbol{x},t)$:*

$$\boldsymbol{v}^{(\hat{\boldsymbol{\nu}})}_{\partial\mathscr{P}}(\boldsymbol{x},t)=\begin{bmatrix}\dfrac{x}{a(t)} & \dfrac{y}{a(t)}\end{bmatrix}^{\mathrm{T}}\frac{\partial a(t)}{\partial t}\,.\tag{68}$$

# B Energy estimate for the bristle deflection

In this Appendix, an upper bound on the total deflection of the bristle is provided using the energy method. For what follows, the boundary $\partial\mathscr{P}$ of the contact patch $\mathscr{P}$ is supposed to evolve smoothly and independently of the bristle deflection[5], and is assumed to be sufficiently regular. Moreover, to lighten the notation, the result is proved using the travelled distance $s$ as independent variable.

Consider a domain $\Omega\subseteq\mathbb{R}^2$. The $L^p$-norm $\|\cdot\|_{L^p(\Omega)}$ $(1\leq p<\infty)$ is defined as [51, 52]

$$\|\cdot\|_{L^p(\Omega)}\triangleq\left(\iint_{\Omega}(\cdot)^p\,\mathrm{d}\boldsymbol{x}\right)^{\frac{1}{p}}.\tag{69}$$

A generic measurable function $f(\cdot)$ is said to belong to the space $L^p(\Omega)$, $1\leq p<\infty$, denoted $f\in L^p(\Omega)$, if $\big\|f(\cdot)\big\|_{L^p(\Omega)}<\infty$. In the following, it is assumed that $u_{\boldsymbol{t}0}(\cdot)\in L^2(\mathring{\mathscr{P}}_0)$. The following result in Proposition B.1 holds true.

[5] This is a very common assumption, albeit not very realistic.

**Proposition B.1** (Energy estimate for the bristle deflection)**.** *Consider the system of PDEs given by Eq. (31), with BC and IC as in Eqs. (8) and (9), respectively. Furthermore, assume that $\bar{\boldsymbol{v}}_{\boldsymbol{t}}(\boldsymbol{x},s)$ is solenoidal and bounded. Then, the following energy estimate holds for the total deflection of the bristle $u_{\boldsymbol{t}}(\boldsymbol{x},s) \triangleq \|\boldsymbol{u}_{\boldsymbol{t}}(\boldsymbol{x},s)\|$:*

$$\left\|u_{\boldsymbol{t}}(\cdot,s)\right\|^2_{L^2(\mathring{\mathscr{P}})} \leq \mathrm{e}^s\left[\left\|u_{\boldsymbol{t}0}(\cdot)\right\|^2_{L^2(\mathring{\mathscr{P}}_0)} + \int_0^s \mathrm{e}^{-s'}\left(\left\|\sigma_x(s') - \varphi(s')y\right\|^2_{L^2(\mathring{\mathscr{P}})} + \left\|\sigma_y(s') + \varphi(s')x\right\|^2_{L^2(\mathring{\mathscr{P}})}\right)\mathrm{d}s'\right], \quad s \in \mathbb{R}_{\geq 0}. \tag{70}$$

*Proof.* First, it may be observed that

$$\frac{1}{2}\frac{\partial u_{\boldsymbol{t}}^2(\boldsymbol{x},s)}{\partial s} = \frac{1}{2}\frac{\partial}{\partial s}\left\|\boldsymbol{u}_{\boldsymbol{t}}(\boldsymbol{x},s)\right\|^2 = u_x(\boldsymbol{x},s)\frac{\partial u_x(\boldsymbol{x},s)}{\partial s} + u_y(\boldsymbol{x},s)\frac{\partial u_y(\boldsymbol{x},s)}{\partial s}. \tag{71}$$

Integrating both sides over $\mathring{\mathscr{P}}$ yields, after some manipulations,

$$\begin{aligned}\frac{1}{2}\frac{\mathrm{d}}{\mathrm{d}s}\left\|u_{\boldsymbol{t}}(\cdot,s)\right\|^2_{L^2(\mathring{\mathscr{P}})} &= \frac{1}{2}\frac{\mathrm{d}}{\mathrm{d}s}\iint_{\mathring{\mathscr{P}}(s)} u_{\boldsymbol{t}}^2(\boldsymbol{x},s)\,\mathrm{d}\boldsymbol{x}\\ &= -\frac{1}{2}\iint_{\mathring{\mathscr{P}}(s)} \bar{\boldsymbol{v}}_{\boldsymbol{t}}(\boldsymbol{x},s)\cdot\nabla_{\boldsymbol{t}} u_{\boldsymbol{t}}^2(\boldsymbol{x},s)\,\mathrm{d}\boldsymbol{x} + \frac{1}{2}\oint_{\partial\mathscr{P}(s)} u_{\boldsymbol{t}}^2(\boldsymbol{x},s)\bar{\boldsymbol{v}}_{\partial\mathscr{P}}(\boldsymbol{x},s)\cdot\hat{\boldsymbol{\nu}}_{\partial\mathscr{P}}(\boldsymbol{x})\,\mathrm{d}L\\ &\quad + \iint_{\mathring{\mathscr{P}}(s)} u_x(\boldsymbol{x},s)\big(\sigma_x(s) - \varphi(s)y\big) + u_y(\boldsymbol{x},s)\big(\sigma_y(s) + \varphi(s)x\big)\,\mathrm{d}\boldsymbol{x}.\end{aligned} \tag{72}$$

Integrating by parts the first integral term on the right-hand side of Eq. (72) and recalling that $\bar{\boldsymbol{v}}_{\boldsymbol{t}}(\boldsymbol{x},s)$ is solenoidal, i.e. $\nabla_{\boldsymbol{t}}\cdot\bar{\boldsymbol{v}}_{\boldsymbol{t}}(\boldsymbol{x},s) = 0$, gives

$$\begin{aligned}\frac{1}{2}\frac{\mathrm{d}}{\mathrm{d}s}\left\|u_{\boldsymbol{t}}(\cdot,s)\right\|^2_{L^2(\mathring{\mathscr{P}})} &= -\frac{1}{2}\int_{\mathscr{T}(s)} u_{\boldsymbol{t}}^2(\boldsymbol{x},s)\big[\bar{\boldsymbol{v}}_{\boldsymbol{t}}(\boldsymbol{x},s) - \bar{\boldsymbol{v}}_{\partial\mathscr{P}}(\boldsymbol{x},s)\big]\cdot\hat{\boldsymbol{\nu}}_{\partial\mathscr{P}}(\boldsymbol{x})\,\mathrm{d}L\\ &\quad + \iint_{\mathring{\mathscr{P}}(s)} u_x(\boldsymbol{x},s)\big(\sigma_x(s) - \varphi(s)y\big) + u_y\big(\boldsymbol{x},s\big)(\sigma_y(s) + \varphi(s)x\big)\,\mathrm{d}\boldsymbol{x},\end{aligned} \tag{73}$$

since either $\boldsymbol{u}_{\boldsymbol{t}}(\boldsymbol{x},s) = \boldsymbol{0}$ on $\mathscr{L}$ or $[\bar{\boldsymbol{v}}_{\boldsymbol{t}}(\boldsymbol{x},s) - \bar{\boldsymbol{v}}_{\partial\mathscr{P}}(\boldsymbol{x},s)]\cdot\hat{\boldsymbol{\nu}}_{\partial\mathscr{P}}(\boldsymbol{x}) = 0$ on $\mathscr{N}$. In this context, it should be also observed that the boundary term on the right-hand side of Eq. (73) is always positive, being by definition $[\bar{\boldsymbol{v}}_{\boldsymbol{t}}(\boldsymbol{x},s) - \bar{\boldsymbol{v}}_{\partial\mathscr{P}}(\boldsymbol{x},s)]\cdot\hat{\boldsymbol{\nu}}_{\partial\mathscr{P}}(\boldsymbol{x}) > 0$ on $\mathscr{T}$. Therefore:

$$\frac{1}{2}\frac{\mathrm{d}}{\mathrm{d}s}\left\|u_{\boldsymbol{t}}(\cdot,s)\right\|^2_{L^2(\mathring{\mathscr{P}})} \leq \iint_{\mathring{\mathscr{P}}(s)} u_x(\boldsymbol{x},s)\big(\sigma_x(s) - \varphi(s)y\big) + u_y(\boldsymbol{x},s)\big(\sigma_y(s) + \varphi(s)x\big)\,\mathrm{d}\boldsymbol{x}. \tag{74}$$

Using Hölder's and then Young's inequality for products yields

$$\begin{aligned}\iint_{\mathring{\mathscr{P}}(s)} u_x(\boldsymbol{x},s)\big(\sigma_x(s) - \varphi(s)y\big)\,\mathrm{d}\boldsymbol{x} &\leq \left\|u_x(\cdot,s)\right\|_{L^2(\mathring{\mathscr{P}})}\left\|\sigma_x(s) - \varphi(s)y\right\|_{L^2(\mathring{\mathscr{P}})}\\ &\leq \frac{1}{2}\left\|u_x(\cdot,s)\right\|^2_{L^2(\mathring{\mathscr{P}})} + \frac{1}{2}\left\|\sigma_x(s) - \varphi(s)y\right\|^2_{L^2(\mathring{\mathscr{P}})},\end{aligned} \tag{75a}$$

$$\begin{aligned}\iint_{\mathring{\mathscr{P}}(s)} u_y(\boldsymbol{x},s)\big(\sigma_y(s) + \varphi(s)x\big)\,\mathrm{d}\boldsymbol{x} &\leq \left\|u_y(\cdot,s)\right\|_{L^2(\mathring{\mathscr{P}})}\left\|\sigma_y(s) + \varphi(s)x\right\|_{L^2(\mathring{\mathscr{P}})}\\ &\leq \frac{1}{2}\left\|u_y(\cdot,s)\right\|^2_{L^2(\mathring{\mathscr{P}})} + \frac{1}{2}\left\|\sigma_y(s) + \varphi(s)x\right\|^2_{L^2(\mathring{\mathscr{P}})}.\end{aligned} \tag{75b}$$

Combining Eqs. (75) with (76) leads to

$$\frac{\mathrm{d}}{\mathrm{d}s}\left\|u_{\boldsymbol{t}}(\cdot,s)\right\|^2_{L^2(\mathring{\mathscr{P}})} \leq \left\|u_{\boldsymbol{t}}(\cdot,s)\right\|^2_{L^2(\mathring{\mathscr{P}})} + \left\|\sigma_x(s) - \varphi(s)y\right\|^2_{L^2(\mathring{\mathscr{P}})} + \left\|\sigma_y(s) + \varphi(s)x\right\|^2_{L^2(\mathring{\mathscr{P}})}. \tag{76}$$

Imposing $\boldsymbol{u}_{\boldsymbol{t}}(\boldsymbol{x},0) = \boldsymbol{u}_{\boldsymbol{t}0}(\boldsymbol{x})$ (and thus also $u_{\boldsymbol{t}}(\boldsymbol{x},0) = u_{\boldsymbol{t}0}(\boldsymbol{x})$) in $\mathring{\mathscr{P}}_0$ and recalling Grönwall-Bellman inequality finally yields the result (70). □

# C Explicit parametrisations of the leading edge when $\varepsilon_x \neq 0$, $\varepsilon_y \neq 0$

When considering a fixed contact patch and a constant nondimensional velocity field as in Eqs. (14) or (33), the definition of the leading edge according to Eq. (6a) combined with Assumption 2.1 yields

$$\mathscr{L} \equiv \left\{ \boldsymbol{x} \in \partial\mathscr{P} \;\middle|\; -\varepsilon_y x + \varepsilon_x y < 0 \right\}. \tag{77}$$

Therefore, depending on the sign of $\varepsilon_x$ and $\varepsilon_y$, the leading edge admits different parametrisations. This appendix reports some possible explicit parametrisation distinguishing amongst four cases.

1. Case $\varepsilon_x > 0$, $\varepsilon_y > 0$:

$$x = x_{\mathscr{L}_1}(y) = \sqrt{a^2 - y^2}, \qquad y \in \Big[-a, a|\varepsilon_y|\Big), \tag{78a}$$

$$x = x_{\mathscr{L}_2}(y) = -\sqrt{a^2 - y^2}, \qquad y \in \Big[-a, -a|\varepsilon_y|\Big). \tag{78b}$$

2. Case $\varepsilon_x > 0$, $\varepsilon_y < 0$:

$$x = x_{\mathscr{L}_1}(y) = \sqrt{a^2 - y^2}, \qquad y \in \Big[-a, -a|\varepsilon_y|\Big), \tag{79a}$$

$$x = x_{\mathscr{L}_2}(y) = -\sqrt{a^2 - y^2}, \qquad y \in \Big[-a, a|\varepsilon_y|\Big). \tag{79b}$$

3. Case $\varepsilon_x < 0$, $\varepsilon_y > 0$:

$$x = x_{\mathscr{L}_1}(y) = \sqrt{a^2 - y^2}, \qquad y \in \Big(-a|\varepsilon_y|, a\Big], \tag{80a}$$

$$x = x_{\mathscr{L}_2}(y) = -\sqrt{a^2 - y^2}, \qquad y \in \Big(a|\varepsilon_y|, a\Big]. \tag{80b}$$

4. Case $\varepsilon_x < 0$, $\varepsilon_y < 0$:

$$x = x_{\mathscr{L}_1}(y) = \sqrt{a^2 - y^2}, \qquad y \in \Big(a|\varepsilon_y|, a\Big], \tag{81a}$$

$$x = x_{\mathscr{L}_2}(y) = -\sqrt{a^2 - y^2}, \qquad y \in \Big(-a|\varepsilon_y|, a\Big]. \tag{81b}$$